J. Fluid Mech. (1992), *vol.* 242, *pp.* 577–609
Printed in Great Britain

The forced turbulent wall jet

By Y. KATZ, E. HOREV AND I. WYGNANSKI†
Department of Aerospace and Mechanical Engineering, University of Arizona, Tucson, AZ 85721, USA

(Received 17 December 1990 and in revised form 28 October 1991)

The effects of external two-dimensional excitation on the plane turbulent wall jet were investigated experimentally and theoretically. Measurements of the streamwise component of velocity were made throughout the flow field for a variety of imposed frequencies and amplitudes. The present data were always compared to the results generated in the absence of external excitation. Two methods of forcing were used: one global, imposed on the entire jet by pressure fluctuations in the settling chamber and one local, imposed on the shear layer by a small flap attached to the outer nozzle lip. The fully developed wall jet was shown to be insensitive to the method of excitation. Furthermore, external excitation has no appreciable effect on the rate of spread of the jet nor on the decay of its maximum velocity. In fact the mean velocity distribution did not appear to be altered by the external excitation in any obvious manner. The flow near the surface, however, (i.e. for $0 < Y^+ < 100$) was profoundly different from the unforced flow, indicating a reduction in wall stress exceeding at times 30%. The production of turbulent energy near the surface was also reduced, lowering the intensities of the velocity fluctuations. External excitation enhanced the two-dimensionality and the periodicity of the coherent motion. Spectral analysis and flow visualization suggested that the large coherent structures in this flow might be identified with the most-amplified primary instability modes of the mean velocity profile. Detailed stability analysis confirmed this proposition though not at the same level of accuracy as it did in many free shear flows.

1. Introduction

The plane turbulent wall jet, evolving over a flat surface in the absence of an external stream is a generic flow governed by the boundary-layer equations. Although this flow has been extensively investigated over the years because of its many engineering applications (see the review articles of Launder & Rodi 1981, 1983) it is still poorly understood. There is a general agreement that the mean velocity in the wall jet is self-similar but the parameters scaling it are controversial (Wygnanski, Katz & Horev 1992) in spite of the massive statistical data available in the literature. The complexity of this flow stems from the fact that its outer part resembles a free jet while its inner part resembles a turbulent boundary layer. In fact most models attempting to predict the average characteristics of the turbulent wall jet superimpose a free jet on top of a boundary layer and match the most obvious boundary conditions.

Experimental investigations of large coherent structures in turbulent shear flows bypassed the wall jet, concentrating either on wall-bounded flows like a boundary layer or a channel (e.g. Willmarth 1975*a*,*b*), or on free shear flows like the mixing

† Also Faculty of Engineering, Tel-Aviv University.

layer, the wake and the jet (e.g. Ho & Huerre 1984; Wygnanski & Petersen 1987). In the latter category of flows, the large coherent structures were identified as the predominant instability modes and were quantitatively analysed in this context. However, the large coherent structures in wall-bounded flows are much more complex and more difficult to identify than in free shear flows. Many forms of such structures have been observed visually (Kline *et al.* 1967; Falco 1977) but no consensus was reached as to their origin and their precise association with the enhancement of the skin friction or with the rate of growth of the boundary layer. Since Hussain & Reynolds (1970, 1972) failed to excite growing two-dimensional modes in a turbulent channel flow, it was tentatively concluded that plane instability modes are not related to the large coherent structures observed in channels and boundary layers. However secondary instabilities, akin to the ones responsible for the generation of hairpin vortices in a laminar boundary layer (e.g. Craik 1985), may still be identified with the creation of large coherent structures in fully turbulent wall-bounded flows. In fact 'sublayer streaks' were recently modelled by Landahl (1990), by using an instability concept associated with three-dimensional intermittent disturbances growing algebraically in the direction of streaming.

Free shear flows are inviscidly unstable, while boundary layers in the absence of an adverse pressure gradient are not. There is enough evidence (Katz, Nishri & Wygnanski 1989) to suggest that a boundary layer on the verge of separation resembles a free mixing layer and its responds to external stimuli, like a mixing layer. The receptivity of this boundary layer is attributed to an inviscid instability which may dwarf, in this case, any other form of instability and generate large, predominantly two-dimensional, coherent structures. The generic wall jet is inviscidly unstable in its outer region and may thus possess large coherent structures characteristic of a plane turbulent jet. The similarity between the outer part of the wall jet and the free jet will be explored in this context and the relevance of the solid surface to the evolution of the large coherent structures will be assessed. From this point of view, the boundary layer in a strong adverse pressure gradient may be regarded as a wake evolving in the vicinity of a solid surface. In both flows the significance of the outer region is accentuated while the no-slip conditions at the solid surface are maintained.

The wall jet might be the ideal flow configuration for resolving the intricate interactions between the outer and the inner structures in a turbulent boundary layer, because it offers a larger degree of flexibility and controllability of flow parameters than a boundary layer does, regardless of pressure gradient. This flexibility stems from the fact that a prescribed jet momentum can be maintained by changing the dimension of the nozzle and the efflux velocity simultaneously. Consequently, one can alter the vorticity in the outer layer without a concomitant alteration in the momentum input which might also change the susceptibility of the wall jet to external perturbations. Embedding the wall jet in an external stream (i.e. creating a tangentially blown boundary layer) increases further the parametric flexibility of this flow by enabling one to change the ratio between the free-stream velocity outside the boundary layer and the jet velocity near the solid surface. Thus the structure of the wall jet can be progressively altered and the importance of the outer vortical layer on the wall region can be evaluated.

In the present report we shall describe the major effects of a harmonic, two-dimensional excitation on the structure of a turbulent wall jet. Although the investigation is mostly experimental, it includes a rudimentary stability analysis in order to quantify the scale and the intensity of the observed large coherent

structures. The experiments were carried out in air, on the simplest wall-jet configuration in the absence of an external stream or surface curvature. The flow was incompressible and the Reynolds numbers based on the efflux velocity and on the nozzle dimension varied between 3×10^3 and 3×10^4.

2. A brief description of the experiment

Although a detailed description of this apparatus has been given by Wygnanski *et al.* (1992, thereafter referred to as WKH) a schematic drawing of it is reproduced here (figure 1) in order to show where and how the wall jet was excited and provide a clear definition of the coordinate system used.

Since the main purpose of this investigation was to determine the receptivity of the wall jet to two-dimensional forcing, the method of forcing, its frequency and amplitude were all considered as variables of potential importance. A thin metal strip spanning the facility was attached to the upper lip of the nozzle with Scotch-tape which also served as a pivot around which the little flap could be deflected. The downstream side of the 6 mm wide flap was attached to a taut piano wire which could oscillate up or down depending on the movement of two shakers mounted outside the facility. The two-dimensional motion of this flap forced the initial shear layer locally, which blended with the outer part of the wall jet further downstream. Another, global method of forcing was provided by the oscillations of the cone of an 8 in. loudspeaker mounted on the wall of the plenum chamber. The jet emerged from a nozzle of width b, with a top-hat velocity profile except for two thin boundary layers, one near the outer lip of the nozzle and the other near the wall. The thickness of both layers increased rapidly in the direction of streaming so that at $X/b = 1$ the potential core had shrunk to approximately 70% of the nozzle dimension which was 5 mm for the data plotted in figure 2. The plenum chamber excitation resulted in a fairly even distribution of oscillations across the entire jet in the plane of the nozzle, while the oscillations produced by the flap resulted in amplitudes which were concentrated near the outer lip of the nozzle and near the solid surface. The boundary layer near the solid surface was very receptive to these oscillations and at $X/b = 1$ the maximum amplitude near the surface exceeded 40% of the amplitude measured in the wake of the flap. It is interesting to note that the mean velocity distribution was almost identical regardless of the method of forcing used. In order to make rational comparisons between the two modes of excitation, the integrated input amplitude across the flow was equated in both experiments. The data presented in figure 2 are an example for which this integral was nominally 5% of the wall-jet exit velocity. This number is considered as the amplitude of the forcing at the nozzle, and it was allowed to vary between 2% and 20%. Although this procedure does not uniquely establish all the aspects of external excitation, it enables one to reduce to two the number of independent parameters associated with the excitation (i.e. amplitude and frequency). The frequency of the forcing expressed in terms of a jet Strouhal number, $St_j \equiv fb/U_j$ varied between 3.4×10^{-3} and 18.3×10^{-3}.

The streamwise component of the velocity was measured with a single hot-wire probe starting some 20 slot widths downstream of the nozzle. Most of the measurements extended beyond 100 slot widths from the nozzle, where the maximum velocity in the wall jet dropped to approximately one quarter of its initial value. The Reynolds number at the nozzle was altered by changing the efflux velocity, U_j, between 10 and 50 m/s and/or by changing the width of the slot, b, between 2.5 and 7.5 mm. The range of Reynolds numbers considered was:

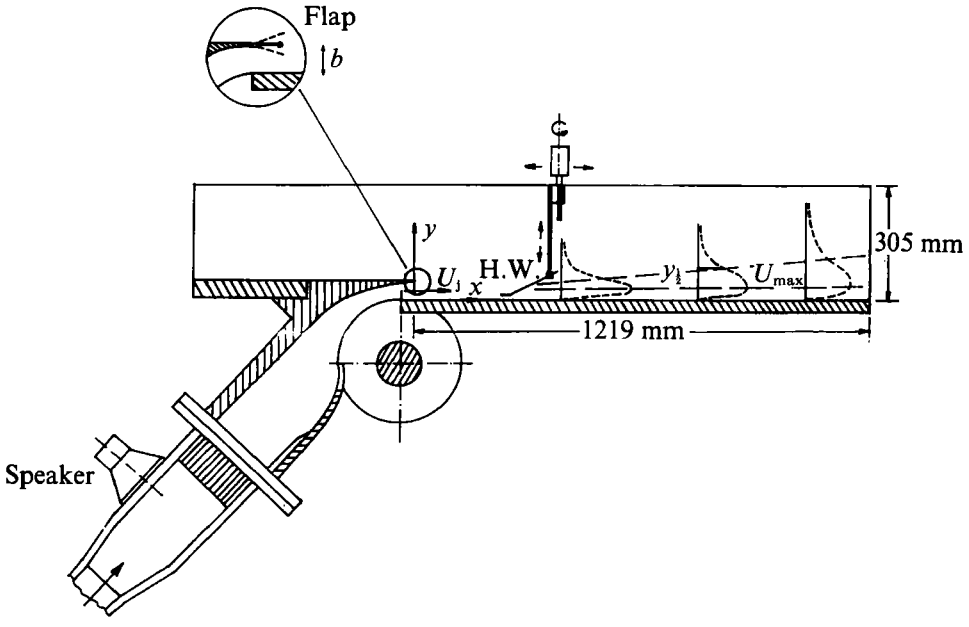

FIGURE 1. A schematic of the wall-jet apparatus.

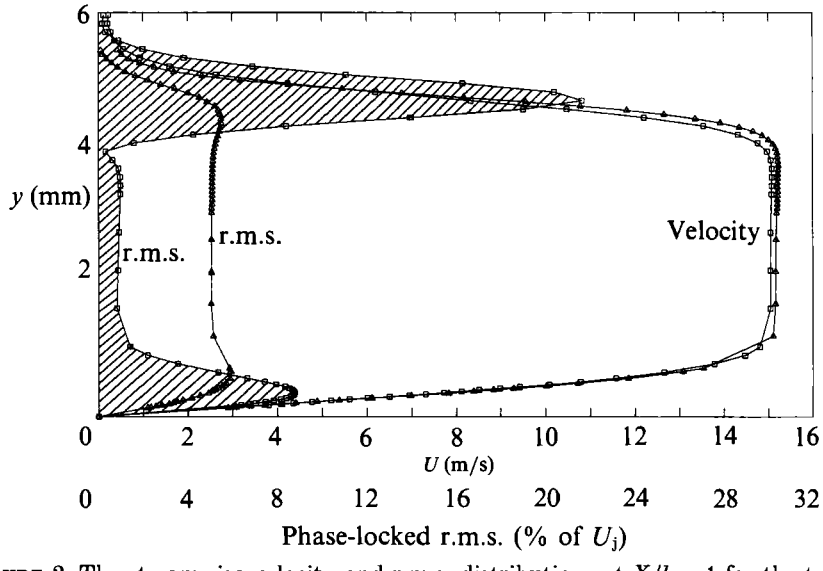

FIGURE 2. The streamwise velocity and r.m.s. distributions at $X/b = 1$ for the two methods of excitation: □, forcing by flap; △, forcing by speaker.

Symbol	U_j (m/s)	b (mm)	Re_j	f(Hz)	$St \times 10^{15}$	r.m.s. (%)
○	10	5	3400	34	444	5
△◁	15	5	5000	34	88	5
✱	15	5	5000	34	88	10
⏢◖	15	5	5000	34	88	20
○○	15	5	5000	5	13	2
◇	15	7.5	7500	15	17	5
⊠	15	7.5	7500	15	17	2
□	30	5	10000	34	5.5	5
⬠⬠	57	5	19000	34	0.4	2
▨▨	57	5	19000	34	0.4	2 (Flap)
☼	15	5	5000	10	25	5 (Flap)
◉◉	15	5	5000	5	13	2 (Flap)

TABLE 1. Symbols used in the figures

$3 \times 10^3 \leqslant Re_j \leqslant 3 \times 10^4$, where $Re_j \equiv U_j b/\nu$. Hot-wire data were acquired and analysed digitally together with an oscillator signal which was used to force the wall jet. This signal also provided a phase reference for the phase-locked data.

3. Experimental results

3.1. *The effects of forcing on Reynolds-averaged quantities*

External excitation of free shear flows, like the mixing layer, has a strong effect on a variety of time-averaged quantities like the mean velocity distribution, the rate of spread of the flow, the turbulent intensity and the Reynolds stress. It is thus natural to start the present discussion of the experimental results by exploring parametrically the effects of forcing on the same quantities in the wall jet.

The mean velocity profile is usually plotted in similarity coordinates in which the velocities measured at a given X-location are scaled by the local maximum velocity U_m, and the distances from the wall are divided by the distance at which the velocity had decreased to half of its local maximum value in the outer part of the flow. The unperturbed wall jet is self-similar because the normalized velocity profiles measured at numerous X-locations collapse onto a single curve irrespective of Reynolds number provided the latter exceeds a certain threshold level.

A variety of forced flows were considered in the present experiment: they differed in jet momentum, slot width, frequency and amplitude of the imposed oscillations, and finally the manner in which forcing was introduced to the flow. Whenever one of the above parameters was changed the entire velocity field had to be mapped. A sample of the data is shown in figure 3. The symbols used in this and subsequent figures are defined in table 1. The velocity profile plotted in figure 3(*a*) exhibits self-similarity with respect to $Y_{m/2}$ and U_m irrespective of the X-location (which was altered between 30 to 120 slot widths) while the profile plotted in figure 3(*b*) proves the existence of self-similarity irrespective of the changes in all other parameters considered. Both profiles are compared to the dimensionless, unforced, velocity profile measured by WKH and represented by a solid curve. One may conclude that two-dimensional external excitation does not affect the normalized form of the velocity distribution within the range of parameters considered. Replotting the velocities adjacent to the wall on an expanded scale (figure 3*c*), and comparing them to unforced velocity measurements at otherwise identical conditions, indicate small

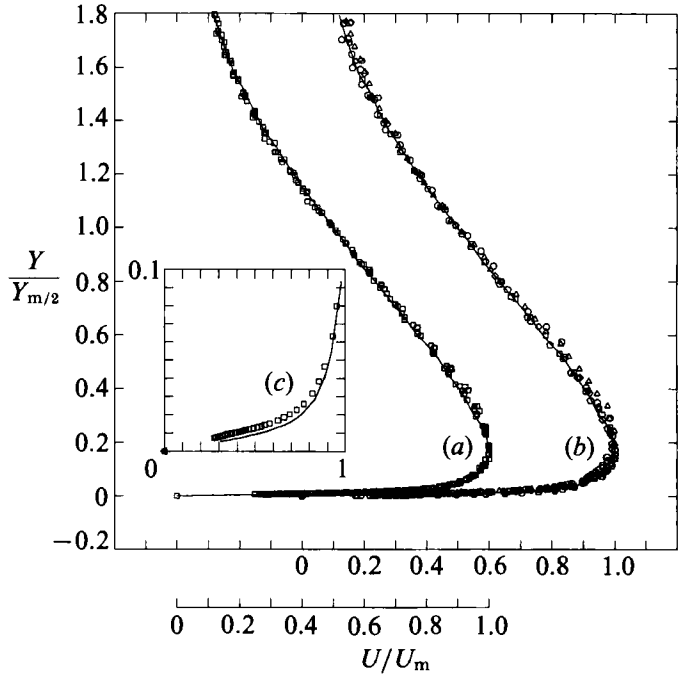

FIGURE 3. Velocity profiles using self-similar coordinates: (*a*) same Re_j, St and forcing frequency but different X-locations; (*b*) various Re_j, jet momenta, amplitudes and frequencies; (*c*) the same as (*a*) but plotted on an expanded scale showing the wall region only. ——, Unforced velocity profile at $U_j = 50$ m/s measured by W, K H. The symbols are defined in table 1.

but consistent differences between the two sets of data. These differences will be discussed later in some detail.

The rate of spread of the wall jet and the rate of decay of its maximum velocity are somewhat affected by the external excitation. These effects, however, are considerably smaller than anticipated on the basis of experience accumulated in free shear flows. The data presented correspond to an initial, average forcing amplitude of 2%, which was the lowest considered here, although it is thought to be high by free jet-flow standards. The rate of spread of the jet was increased slightly owing the excitation, particularly when compared to the unforced flow at higher nozzle Reynolds numbers (figure 4*a*), while the rate of decay of U_m increased more effectively at lower Re_j (figure 4*b*). The solid lines in this figures represent a linear least-square fit to the present data, while the dashed lines provide a comparison with the unforced flow. Alternative methods of forcing (i.e. flap or plenum chamber excitation) had a minimal impact on either quantity plotted in figure 4. When the ratio $[U_j/U_m]^2$ is plotted against the dimensionless distance from the virtual origin of the flow, the data are reasonably well represented by a straight line, suggesting that the approximate decay of the maximum velocity is proportional to $(X-X_0)^{-1}$ regardless of forcing. The virtual origin was defined by requiring that the extrapolated value of $(U_j/U_m)^2 = 1$ in the plane of the nozzle. In the specific case shown the data representing the local width of the flow $Y_{m/2}$ may also be extrapolated to $Y_{m/2} = b$ at $X = 0$ but this was not the criterion used in determining the virtual origin. On the basis of the data shown in figure 4 one may conclude that the effect

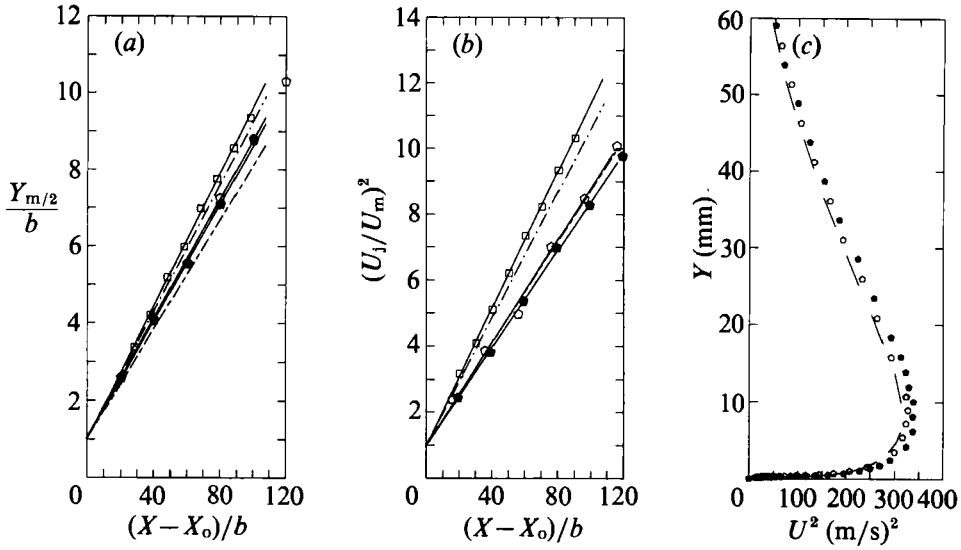

FIGURE 4. The effects of forcing on Reynolds-averaged quantities: (*a*) the evolution of the width of the wall jet with X; (*b*) the decay of the maximum velocity with X; (*c*) a local distribution of the square of the mean velocity. ----, Unforced; ——, linear least-square fit.

of Re_j on the mean velocity distribution in the wall jet is much more significant than the effects of external excitation.

Plotting the square of the mean velocity profile in *dimensional* coordinates (figure 4*c*) suggests that the externally excited jet retains more of its initial momentum at a given cross-section than the regular, unforced, wall jet. Furthermore, if one recalls that the average turbulent wall jet loses less than 8% of its initial momentum up to $X/b = 100$ (see Launder & Rodi 1981, p. 83) then the seemingly small differences between the momentum contained in the forced and unforced wall jets become considerably more significant. These differences disappear as a consequence of the normalization used in the quest of showing self-similarity (figure 3*a*,*b*). We may conclude that the local width of the wall jet and its local maximum velocity are much less receptive to external excitation than the comparable quantities in the free jet.

A more appropriate comparison (figure 5) uses the variables suggested by Narasimha, Narayan & Parthasarathy (1973) and by WKH for the unforced wall jet because then the data are not contaminated by the effects of Reynolds number. In this case the dependent variables describing the mean velocity field:

$$U_m \nu/J, \quad Y_{m/2} J/\nu^2,$$

are functions of a single independent variable $\xi \equiv XJ/\nu^2$, where $J = [U_j^2 b]$, ν is the kinematic viscosity of the fluid, and X is the actual distance from the nozzle (because the distance between the nozzle and the virtual origin is, in most cases, negligible in comparison with X).

The solid lines drawn in figure 5 represent the unforced data accumulated for $Re_j \geqslant 7500$ while the broken lines correspond to $Re_j \leqslant 5000$. The symbols plotted in figure 5(*a*,*b*) represent data corresponding to various frequencies of excitation at nozzle Strouhal numbers ($St_j \equiv fb/U_j$) of $3 \leqslant St_j \times 10^3 \leqslant 17$ (corresponding to $St \equiv f\nu^3/J^2$ of $0.4 \leqslant St \times 10^{15} \leqslant 444$) and amplitudes, based on the streamwise velocity perturbation near the nozzle, ranging from 2% to 20%. Although some

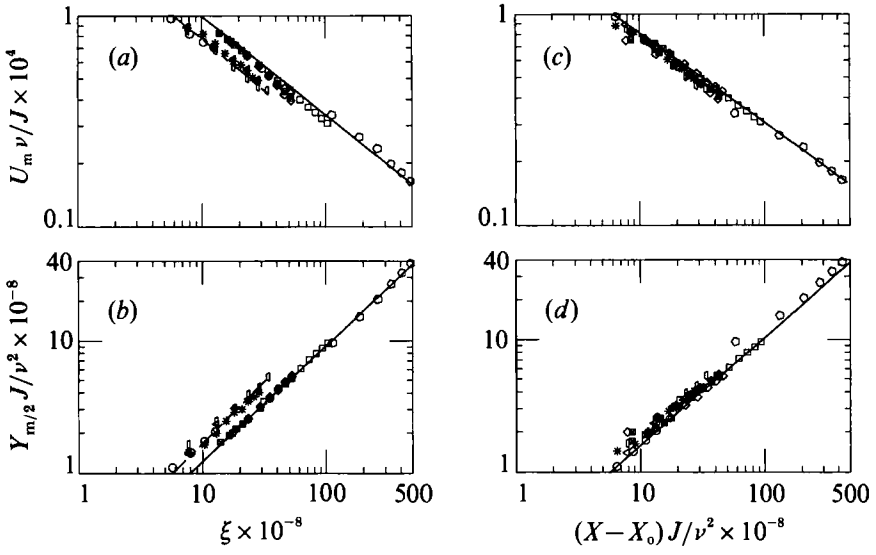

FIGURE 5. The effects of forcing on U_m and $Y_{m/2}$ as functions of ξ: (*a*) the maximum velocity of the jet; (*b*) the width of the jet; (*c*) the same as (*a*) but X is measured from the virtual origin; (*c*) the same as (*b*) but X is measured from the virtual origin. ---, Unforced data $Re_j = \geqslant 7500$; ——, $Re_j \leqslant 5000$.

consistent differences depending on the level of forcing and on the Strouhal number can be detected they do not alter our initial conclusion about the lack of sensitivity of these mean-flow parameters to the external excitation. The cumulative effect of the threshold in Re_j which is associated with transition in the nozzle and occurs around $Re_j \approx 5000$ appears to be much more significant than the effect of the two-dimensional excitation. In the unforced case, this dependence on the threshold value in Re_j was essentially eliminated by accounting for the virtual origin of the flow which shifted downstream at higher Reynolds numbers. In fact, one may replot the data shown in figure 5(*a*, *b*) against a new dimensionless distance measured from the virtual origin (i.e. $(X-X_0)J/\nu^2$) and ignore the effects of forcing on the rate of spread (figure 5*c*, *d*) although the apparent scatter suggests that the mean flow might be weakly dependent on external excitation. One should remember that the data are plotted on a compact logarithmic scale because of the 'power-law' dependence of U_m and $Y_{m/2}$ on ξ. Dimensional analysis of the independent parameters in the externally excited wall jet suggests that variables other than ξ might affect the mean velocity distribution. Whenever the external excitation is harmonic, the broadening or the distortion of mean flow will depend on the square of the local amplitude of the velocity perturbations. In some cases the finite amplitude might be introduced directly by the forcing mechanism, while in others the flow itself might act as an amplifier. Before exploring the specific effects of the amplitude and the frequency of the excitation on the rate of spread of the wall jet we shall examine the global effect of the excitation on the loss of momentum resulting from skin-friction drag.

The velocities plotted in figures 3(*c*) and 4(*c*) suggest that forcing the wall jet might have an effect on the drag. Since the local skin friction is most conveniently determined from the slope of the mean velocity profile near the wall (WKH), the procedure was repeated here in spite of the fact that it is not considered in the literature as being very reliable (see also Launder & Rodi 1981). The velocity

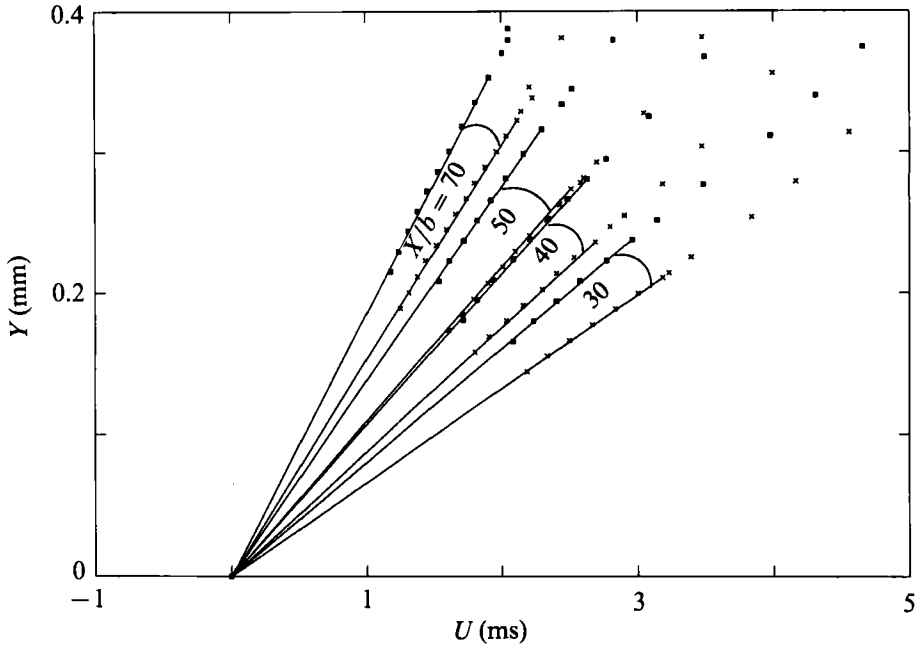

FIGURE 6. The effect of forcing on dU/dY near the wall; ×, unforced; ⊠, forced. $St \times 10^{15} = 17$, $Re_j = 7500$.

measurements plotted in figure 6 are shown in dimensional form because this representation enables the reader to assess the quality and the amount of data acquired in the viscous sublayer. Sometimes more than 10 data points were included in the linear fit made to the velocity profile near the wall. There is no doubt that even a relatively low level of forcing (the data plotted correspond to an initial amplitude of 2%) results in a reduction of the wall shear stress, τ_w. Heat loss from the hot wire to the wall was negligible since the flow was turbulent and most of the data were taken at distances from the wall ranging from 50 to 80 wire diameters while Re based on the wire diameter varied from 0.7 to 4 (see Wills 1962).

Plotting $\tau_w/\rho(\nu/J)^2$ versus ξ and comparing the results with the skin friction measured in the absence of forcing indicates clearly the differences in τ_w in spite of the logarithmic scale chosen (figure 7). At no instance did τ_w increase above its nominal unforced value. Reductions in the skin friction of approximately 10% were prevalent at most frequencies corresponding to initial excitation amplitudes that were lower than or equal to 5%. However, reductions in τ_w of approximately 40% were also recorded by forcing at much higher amplitudes corresponding to 10% or 20% of the efflux velocity at the nozzle. Alternatively, forcing at a preselected frequency which is amplified by the flow may achieve the same drag reduction at a much lower input amplitude (figure 7).

In attempting to sort out the independent contributions of frequency (i.e. $St \equiv f\nu^3/J^2$), amplitude and Reynolds number on the local τ_w, one may assume that the dimensionless $(\tau_w/\rho(\nu/J)^2$ depends on the distance from the nozzle (XJ/ν^2) and the local amplitude of the coherent and perhaps quasi-two-dimensional perturbation present locally in the flow. Neglecting the effects of Re_j might be justified on the basis of the correlations derived for the unforced wall jet, but by neglecting the effects of

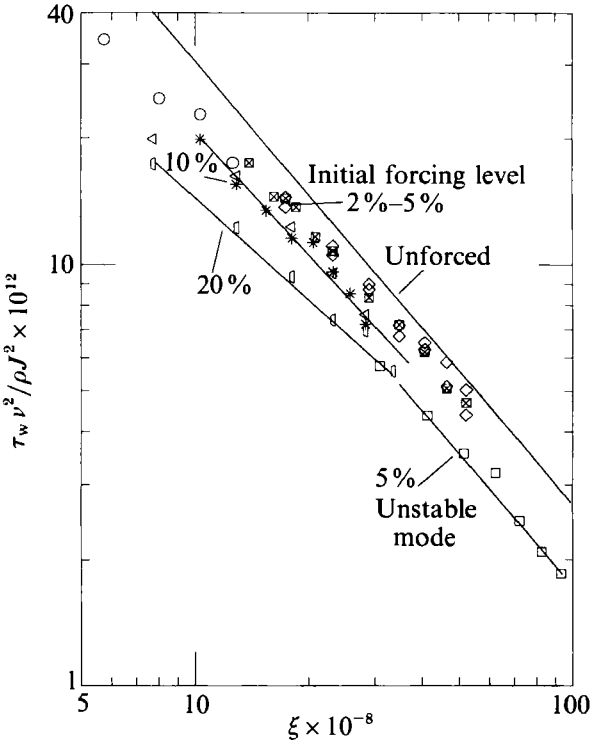

FIGURE 7. The evolution of the dimensionless skin friction with ξ for various Reynolds numbers, Strouhal numbers and forcing amplitudes.

St one tacitly assumes that large two-dimensional coherent structures are similar regardless of their size and origin provided their local intensity is accounted for in some manner. This is a crude assumption which might correlate the distortion of the velocity profile near the surface and the Reynolds stress in the wall region with some (as yet unknown) universal coherent motion.

We computed the phase-locked ensemble-averaged velocity signals and from them deduced the local r.m.s. levels of the coherent motion. These quantities were then integrated across the flow to provide a measure of the intensity of the coherent motion at a given X-station:

$$\langle A \rangle = \frac{1}{U_j Y_{0.1}} \int_0^{Y_{0.1}} \left[\frac{1}{T} \int_0^T [\langle U \rangle - \langle \bar{U} \rangle]^2 \, \mathrm{d}t \right]^{\frac{1}{2}} \mathrm{d}Y, \tag{3.1}$$

where $\langle U \rangle$ is the phase-locked velocity at a given Y and

$$\langle U \rangle = \frac{1}{T} \int_0^T \langle U \rangle \, \mathrm{d}t,$$

$Y_{0.1}$ is the distance from the wall to the location at which $U/U_m = 0.1$ at the outer region and T is the period of the forcing signal.

Some of the data sets shown in figure 7 were calculated as functions of the computed local amplitudes and then replotted again with ξ as the abscissa and with the local, cross-flow-averaged r.m.s. values of the coherent motion as parameters

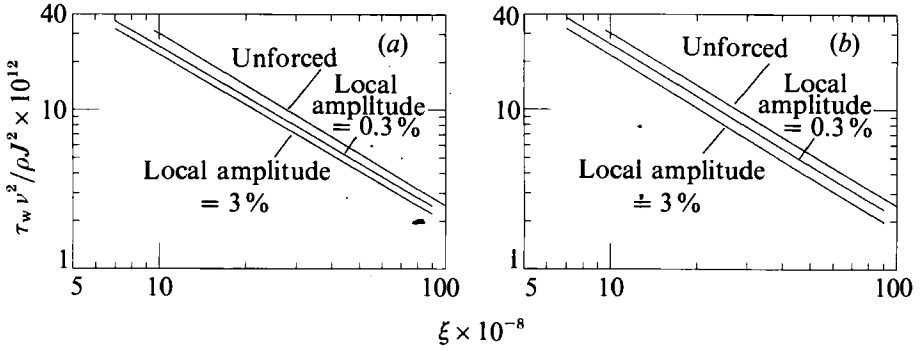

FIGURE 8. The evolution of the dimensionless skin friction with ξ where (*a*) the r.m.s. value of the coherent motion is a parameter; (*b*) the coherent signal at the forcing frequency is a parameter.

(figure 8*a*). One may deduce from this figure that a local coherent motion having an average amplitude of 0.3% may be responsible for a reduction in τ_w of approximately 15% while an additional increase in local amplitude by a factor of 10! (i.e. to 3% of U_j) resulted in an incremental reduction in $(\tau_w)/\rho(\nu/J)^2$ of an additional 15% only. This suggests that the reduction in the local skin friction is not linearly dependent on the strength of the coherent motion as defined by the single parameter $\langle A \rangle$.

Fourier decomposition of the coherent signal prior to integration across the flow and a repetition of the procedure mentioned above at the forcing frequency correlates the dependence of $(\tau_w)/\rho(\nu/J)^2$ on the coherent amplitude of the motion at this frequency (figure 8*b*). It appears that when the local amplitudes of the coherent oscillations at the forcing frequency are also 0.3%, the reduction in τ_w is also 15%, but a further increase in that amplitude to 3% resulted in even smaller reduction in τ_w than estimated for the overall coherent signal. Since the difference in the estimation of τ_w between processing the broadband coherent signal or the coherent signal at the forcing frequency is small, one may attribute most of the reduction in τ_w to the forcing frequency.

Isolating the effect of frequency on τ_w is not a simple task. A typical wavelength associated with the forcing should be proportional to U_m/f which might be expressed in terms of the independent variables J and ν as $\lambda \propto J/\nu f$. Since the characteristic width of the flow, $Y_{m/2}$, is proportional to ν^2/J the dimensionless ratio between these two lengthscales is

$$St^* \equiv (f\nu^3/J^2) \times 10^{15}$$

as might have been deduced from dimensional analysis applied to the fully developed wall jet (see WKH). However, when λ becomes either comparable to the slot width, or to a characteristic length of the apparatus one ought to be concerned with these dimensions. In the first instance the details of the flow near the nozzle might affect the streamwise evolution of the jet, while in the second case the flow leaving the apparatus (i.e. the outflow conditions) might be of significance. By changing either the jet momentum or the slot width while holding the forcing frequency constant one alters not only the Strouhal number but the Reynolds number as well. Although each of these variables might affect τ_w in a different way we may presume that the effect of Re_j would be small provided the usual threshold value of Re_j was exceeded.

Inviscid amplification of two-dimensional disturbances in free shear flows occurs wherever the local wavelength of the disturbance is commensurate with the thickness

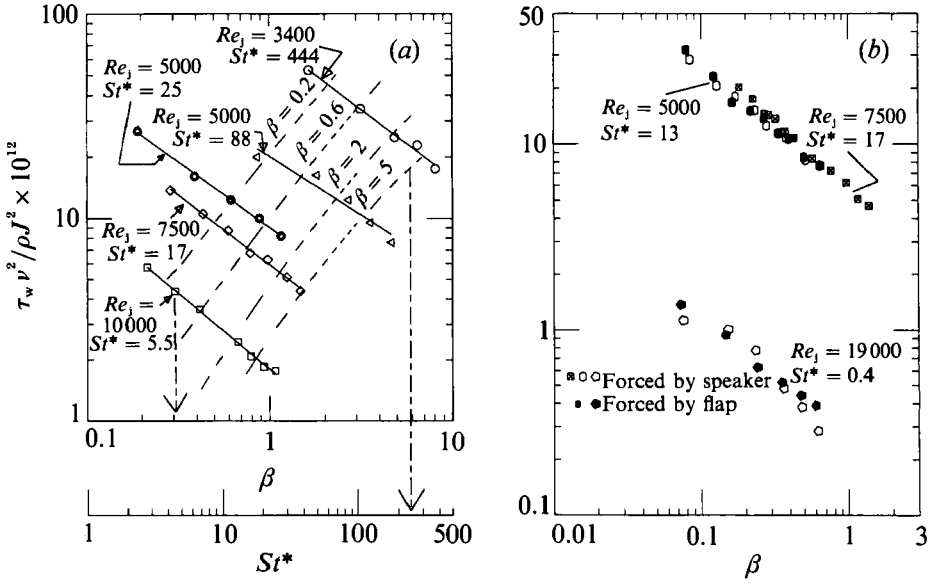

FIGURE 9. The dependence of the dimensionless skin friction on the dimensionless frequency β when St is a parameter or on St when β is a parameter: (*a*) corresponds to a forcing amplitude of 5% and (*b*) to a forcing amplitude of 2%.

of the flow. In the context of the present definition of the characteristic velocity and lengthscales, the maximum amplitude attainable at a prescribed streamwise location for a given excitation level should depend on

$$\beta \equiv 2\Pi f Y_{m/2}/U_m,$$

which is commonly used in hydrodynamic stability. In fact, a linear stability model applied to the wall jet suggests that all frequencies below $\beta \approx 0.67$ are amplified at sufficiently high Reynolds number. Consequently the dimensionless τ_w, which also depends on the local amplitude of the perturbations, was plotted as a function of β. It is self-evident that β depends on the imposed frequency and on X ($\beta \propto X^{1.35}$; see WKH) and therefore represents a product of two independent parameters.

All the data presented in figure 9(*a*) were taken at a single initial excitation level of 5% and in figure 9(*b*) of 2%. Each set of measurements (connected by a solid line in figure 9*a*) corresponds to a prescribed St^* and to a constant value of Re_j. One may observe that for a given set of initial conditions (i.e. prescribed J, ν, ρ, f and a constant imposed amplitude) the local value of $(\tau_w)/\rho(\nu/J)^2$ depends on β and therefore, at a constant St^*, $(\tau_w)/\rho(\nu/J)^2$ decreases with increasing X (i.e. increasing β). The role of Re_j appears to be minor, as might be recognized by comparing two sets of data taken at different Re_j (5000 and 7500) but only slightly different St^* (figure 9*b*), or at a constant $Re_j = 5000$ but a very different St^* ($St \times 10^{15} = 25$ and 88; figure 9*a*). The data plotted in figure 9(*b*) may also serve as proof that τ_w is independent of the method of forcing because all filled symbols in this figure represent the method of shear-layer excitation using the flap, while all other symbols represent the global plenum-chamber excitation. Furthermore, since the results corresponding to an initial forcing level of 2% can hardly be distinguished from comparable data obtained at a forcing level of 5% (at identical values of St^*), one may suggest that

the flow is not very sensitive to differences in the initial amplitude levels in the range of amplitudes considered.

Each solid line in figure 9(*a*) reflects the dependence of τ_w on X; the vertical displacement of these lines at a prescribed J/ν reflects the dependence of τ_w on the frequency of the imposed oscillations. It appears that the lowest possible frequency of forcing is most effective in reducing the local τ_w at a predetermined streamwise location (i.e. at some prescribed $Y_{m/2}$ and U_m). One may cross-plot the local dimensionless τ_w using β as a constant parameter with St^* as an abscissa (the broken lines in figure 9*a* represent constant value of β and should be looked at in conjunction with the lower scale representing St^*). This plot enables one to observe the dependence of $(\tau_w)/\rho(\nu/J)^2$ on St^* for a prescribed amplification rate of the disturbance which uniquely depends on the value of β provided the process is linear. For small values of β, one may fit straight lines, which have an approximate slope of unity, to the curves β = constant and thus conclude that for a constant rate of amplification:

$$\tau_w/\rho = f\nu + \text{const.}$$

Although both the validity and the accuracy of this relationship are limited, it may serve as a first-order approximation in assessing the dependence of the local skin friction on frequency in a two-dimensionally forced wall jet. It is interesting to note that the lowest St at which excitation has an effect on drag was not reached in the present experiment.

Given the sensitivity of τ_w to the local amplitude of the phase-locked disturbance (figure 8), one could expect an adverse effect on τ_w wherever β exceeds the value corresponding to the amplified frequency of the imposed oscillations (i.e. the neutral point on the linear stability diagram) because thereafter the amplitude of the waves would have to decrease. This might have been the case if β were independent of X and the amplification process were entirely linear. The observed reduction of the skin friction may be partly attributed to nonlinear processes associated with the generation of a subharmonic frequency which was clearly observed at large distances from the nozzle. The interaction with the incoherent Reynolds stresses might also had some effect on the final outcome.

The fractional loss of momentum in the direction of streaming is equal to frictional losses integrated over a prescribed distance:

$$\frac{1}{J}\int_{X_0}^{X}\frac{\tau_w}{\rho}\,dX = \int_{\xi_0}^{\xi}\frac{\tau_w}{\rho}\left(\frac{\nu}{J}\right)^2 d\xi. \tag{3.2}$$

Since the prediction of drag and its possible reduction by active means is of primary interest to the practising engineer, this quantity is plotted *vs.* the physical distance X/b (figure 10), knowing full well that Re_j becomes an important factor in this plot. It was decided to begin the calculations from $X/b = 30$, where the wall jet was fully developed. Four cases are plotted in figure 10 ranging in St from 444×10^{-15} to 5.5×10^{-15} and in Re_j from 3400 to 10^4 respectively. The amplitude of forcing was maintained at 5% throughout but the slot width was maintained at 5 mm in figures 10(*a*, *b*, *d*) while being increased to 7.5 mm in figure 10(*c*). This change in the slot width implies that the data shown in figure 10(*c*) correspond to a physical distance which is 50% larger than in the rest of the plots. The dimensionless distance ξ is shown above each figure for reference. The vertical distance between the curve representing the forced data and the unforced one corresponds to actual drag

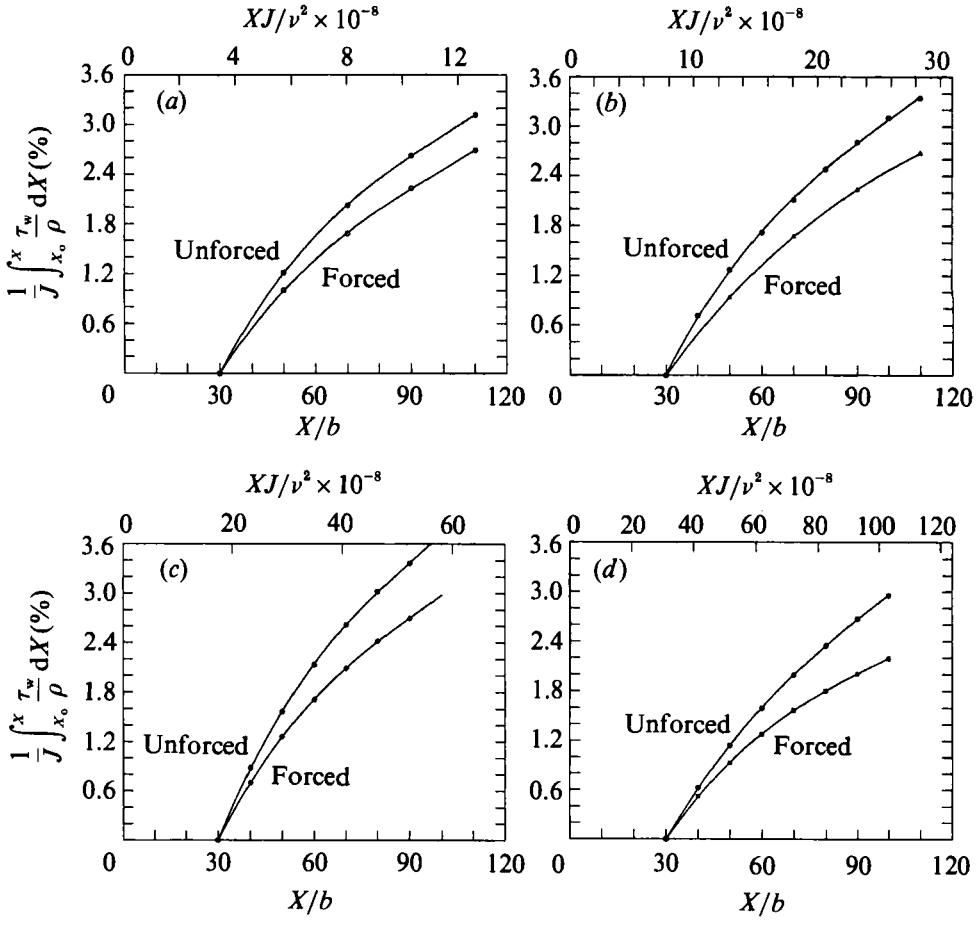

FIGURE 10. The overall drag reduction due to external excitation: (*a*) $Re_j = 3400$, $St \times 10^5 = 444$; (*b*) $Re_j = 5000$, $St \times 10^{15} = 88$; (*c*) $Re_j = 7500$, $St \times 10^{15} = 17$; (*d*) $Re_j = 10000$, $St \times 10^{15} = 5.5$.

reduction due to forcing. By comparing these differences at $X/b = 100$ and normalizing the data by the local unforced values of momentum loss one gets a drag reduction of 15% corresponding to the case plotted in figure 10(*a*); 19% in (*b*); 22% in (*c*) and 27% in (*d*). These results reinforce our previous conclusion that most efficient drag reduction is obtained by low-frequency forcing.

A comparison was made between the mean velocity distributions of the forced and the unforced wall jets in the vicinity of the surface by using the conventional 'wall coordinates'. Velocity profiles corresponding to three of the five sets of data shown in figure 9 (i.e. at $St \times 10^{15} = 444$, 88, 5.5 and $Re_j = 3400$, 5000 and 10000 respectively) are plotted in figure 11 on a semi-logarithmic scale. The ordinate of each family of profiles was shifted to provide a clearer visual assessment of the effects of forcing. Since each of the measured velocities was rendered dimensionless with respect to the local friction velocity $U_\tau \equiv (\tau_w/\rho)^{\frac{1}{2}}$, one expects that the effects of forcing on the velocity distribution will correlate with the effects of forcing on τ_w. This proved to be the case because the average reduction in τ_w corresponding to $St \times 10^{15} = 444$ was 15% while for $St \times 10^{15} = 5.5$ it was 34% (see also figure 7), which manifested itself in the largest disparity between the forced and the unforced

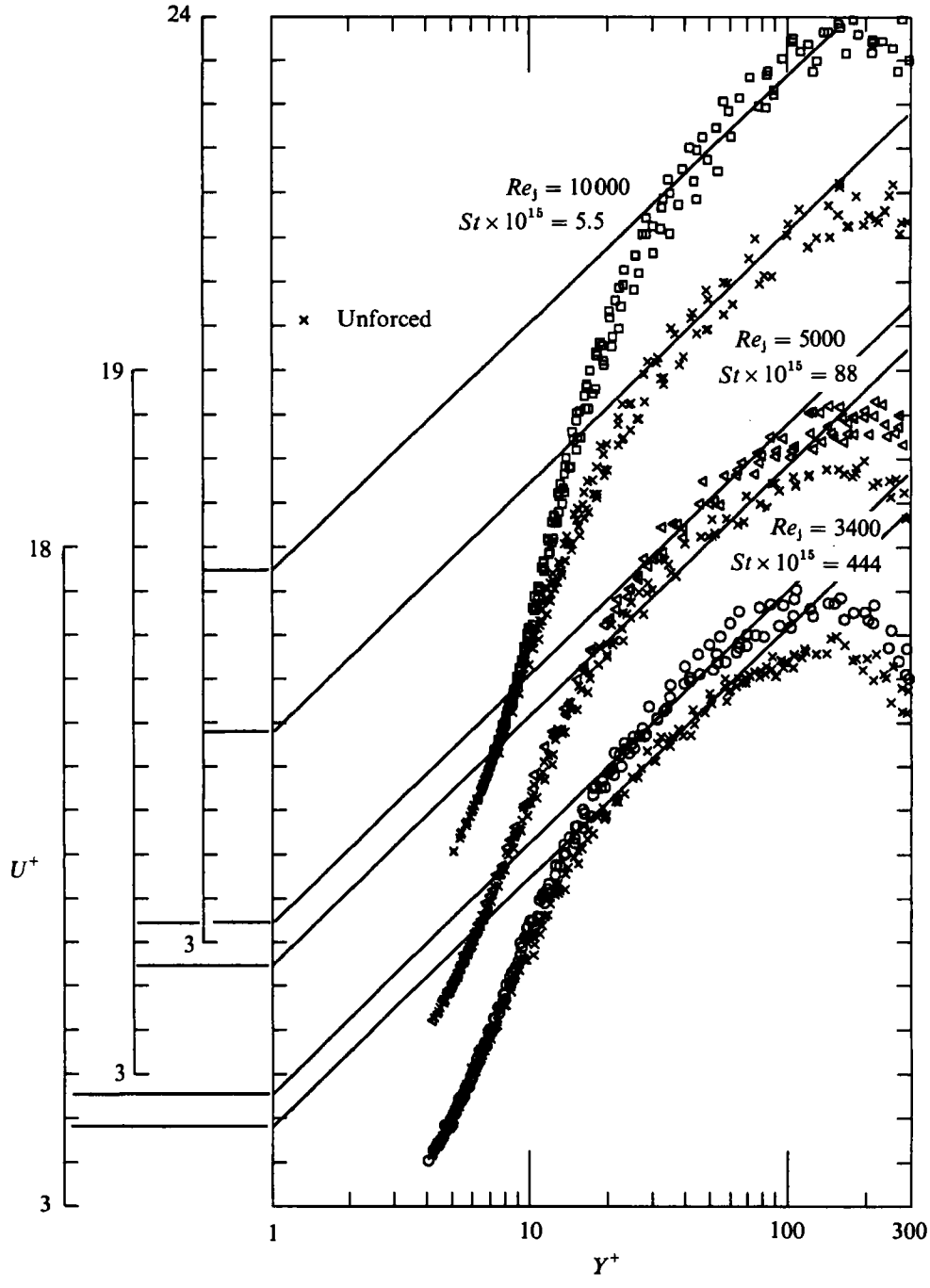

FIGURE 11. The mean velocities in the inner part of the wall jet plotted in wall coordinates.

velocity distributions. It seems that external excitation modifies the velocity distribution in what appears to be the logarithmic region although the existence of such region in the range of Re considered is doubtful. WKH had shown that the slope, A, of the logarithmic profile ($U^+ = A \log Y^+ + B$, where $U^+ = U/U_\tau$ and $Y^+ = YU_\tau/\nu$) appears to be a universal constant and is equal to 5.5, while the additive constant B

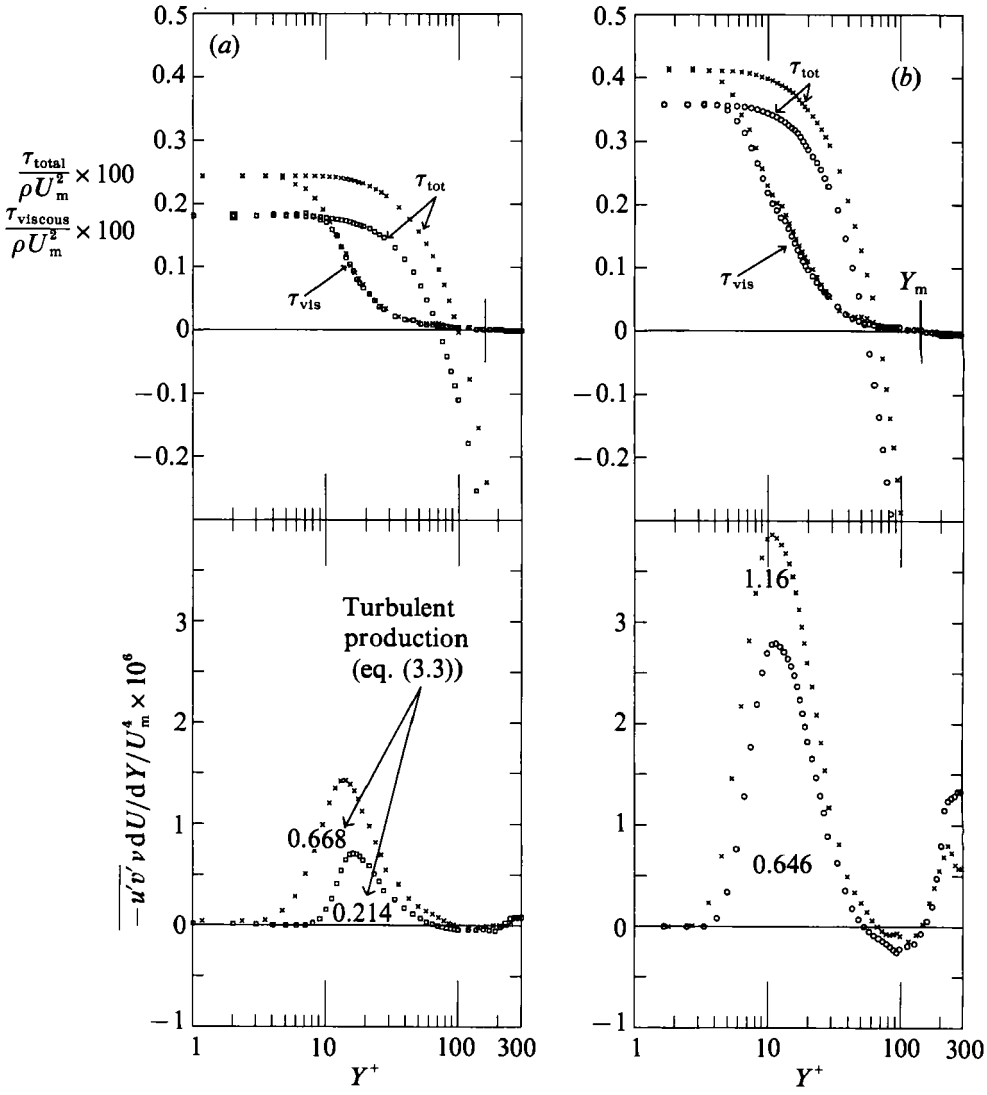

FIGURE 12. The total and viscous shear stress distribution and the turbulent kinetic energy production near the surface: (*a*) $Re_j = 10000$; $X/b = 70$, $St \times 10^{15} = 5.5$; (*b*) $Re_j = 3400$, $X/b = 50$, $St \times 10^{15} = 444$. ×, Unforced; □, forced.

was strongly dependent on Reynolds number. This conclusion applies to the forced wall jet as well. It also appears that the logarithmic fit to the forced data may only be applied at larger values of Y^+ than for the unexcited flow.

WKH showed that some of the underlying assumptions used in deriving the logarithmic velocity profile cannot be applied to the wall jet which they had investigated (i.e. that neither is the logarithmic region far removed from the location at which $Y = Y_m$ nor is the stress constant within that region). Consequently the existence of the logarithmic region appears to be somewhat fortuitous. The introduction of forcing did not only affect τ_w but also reduced the extent of the constant-stress layer (figure 12). The total and the viscous stress distributions in the inner part of the wall jet are plotted at the top of this figure in order to assess the

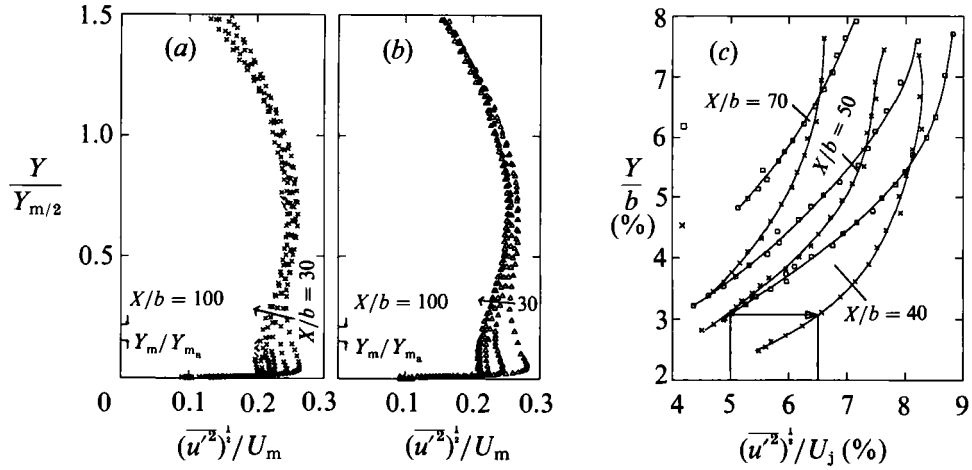

FIGURE 13. The distribution of $(\overline{u^2})^{\frac{1}{2}}$ across the flow: (*a*) for the unforced jet; (*b*) for the forced jet, $St \times 10^{15} = 88$, $Re_j = 5000$; (*c*) a comparison of both cases in the vicinity of the wall: □, forced, $St \times 10^{15} = 5.5$, $Re_j = 10000$; ×, unforced.

effects of excitation on these quantities. The wall stress, which is entirely viscous at the surface, is reduced by the two-dimensional forcing. However for $Y^+ > 10$, the effect of excitation on the viscous stress vanishes since forcing ceases to have an effect on the mean velocity profiles in this region and thus on $\nu(\partial U/\partial Y)$. At $Y^+ > 30$ where the contribution of the viscous stress to the total stress becomes vanishingly small, the latter decreases rapidly with increasing distance from the wall and changes sign between $60 < Y^+ < 100$ depending on the forcing and on Re_j.

The lateral distribution of turbulent energy production, $-(u'v')\,\partial U/\partial Y$, with increasing distance from the surface is also plotted on figure 12 for the two examples considered above. It is clear that external excitation reduces the Reynolds stress and with it the turbulent production. The integrated turbulent production in the inner region of the wall jet between the surface and the location at which $Y = Y_m$ is defined by

$$\text{Production} = \frac{1000}{(U_m)^3}\int_0^{Y_m} -(u'v')\frac{\partial U}{\partial Y}\,dY. \tag{3.3}$$

For $St = 5.5$ at $X/b = 70$ forcing reduced the value of the production integral from 0.668 to 0.214 while for $St = 444$ and $X/b = 50$ the production integral was reduced from 1.16 in the unforced case to 0.646. This is a significant effect which presumably alters the entire turbulent energy balance in this flow and not just the scales of the large coherent eddies. Since the mean velocity gradient vanishes at $Y^+ \approx 150$, the Y-locations at which $u'v' = 0$ and at which $\partial U/\partial Y = 0$ do not coincide, leading to a region of a weak but negative turbulent production just below the location at which $Y = Y_m$ (see also Kruka & Eskinazi 1964).

No significant difference attributed to forcing could be seen in the level or in the distribution of the longitudinal component of the velocity fluctuations, when the latter are plotted in traditional similarity coordinates spanning the wall jet (i.e. $0 \leqslant Y/Y_{m/2} \leqslant 1.5$; see figure 13*a*, *b*). In view of the lack of self-similarity in the unexcited flow which is most noticeable in the wall region (figure 13*a*), one is obliged to assess the effects of forcing at some prescribed values of ξ (or X/b) for the same efflux conditions at the nozzle. In order to avoid differences in the value and location

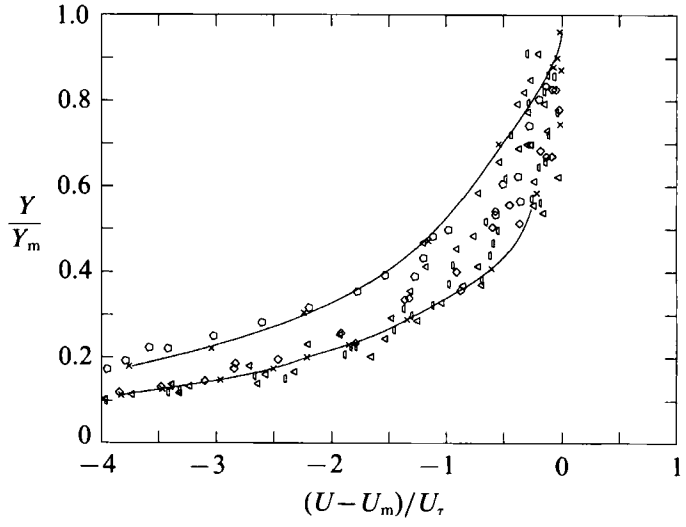

FIGURE 14. The applicability of the 'defect-law' to the forced wall jet.

of U_m, the results shown in figure 13(*c*) are normalized by the conditions at the nozzle. Forcing the wall jet reduces the turbulent intensity in the vicinity of the surface and this reduction is strongly affected by St while all other parameters are maintained constant. The reduction in u'/U_j in some places exceeds 25% as may be deduced from figure 13(*c*) (see the arrow comparing one data point at $X/b = 40$ and $St = 5.5$ which provides an example). Since the production of turbulence increases the level of u', the reduction in u' due to forcing might be a direct result of the reduced production level near the wall.

The velocity defect law is not affected by the external excitation, as may be observed from the plot showing the variation of $(U-U_m)/U_\tau$ with distance from the surface (figure 14). The solid lines plotted in the figure represent the scatter measured in the absence of forcing, while the symbols correspond to a variety of forced conditions. Consequently, even in these highly stretched coordinates, no differences and no particular trends could be detected in the velocity defect laws.

3.2. *Visual identification of large coherent structures*

In order to observe large coherent structures in the fully developed region of the wall jet (i.e. at $X/b > 30$) tracer particles have to be introduced near the nozzle. Otherwise, the turbulent flow inside the jet and the irrotational flow in its neighbourhood, which are both unsteady, will disperse the tracer particles in a random fashion, not allowing them to organize into visible streaklines. Consequently, the width of the slot has to be small, because we are not interested in seeing the structures generated by the mixing layer, and the efflux velocity has to be large, because we want the flow to be turbulent. These conditions impose severe restrictions on the type of flow visualization which can be used, eliminating some of the most convenient techniques. The smoke wire for instance, could not be used near the nozzle, since it could not provide a sufficient concentration of tracer particles required in the high-velocity stream.

By introducing concentrated smoke into the entrained fluid upstream of the nozzle, while the turbulent wall jet was forced, we could observe the existence of

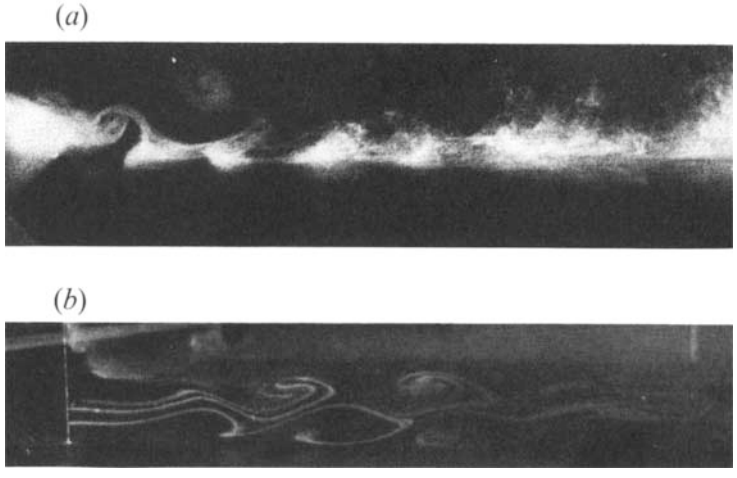

FIGURE 15. Flow visualization of the forced wall jet: (*a*) large coherent structures in the turbulent wall jet; (*b*) instabilities of the laminar wall jet.

coherent structures (figure 15*a*) in the developed region of the flow at $Re \approx 5000$. The Kelvin–Helmholtz instability prevailing in the mixing layer occurring near the outer lip of the nozzle, caused the entrained smoke to roll into a large eddy as it does in the classical mixing layer. Thereafter, the smoke particles were swept towards the wall as a result of the negative vorticity existing in the boundary layer and thus the streaklines appeared to have crept upstream relative to their position far away from the surface. If the same experiment were repeated in a free jet, the particles approaching the core would have been swept downstream as a result of the faster advection in the core region. The particles were then ejected away from the surface into the outer jet zone of the wall jet, forming a second eddy characteristic of a plane jet or a mixing layer (a weak trace of this second eddy can actually be observed in the photo). Smoke concentrations distributed at regular intervals, corresponding to the wavelength associated with the periodic sweeps near the wall, are visible at larger distances from the nozzle. The periodicity of these sweeps suggests that the wall jet is susceptible to external excitation and it contains coherent structures which combine the characteristics of a plane jet and a boundary layer.

The instabilities in the laminar wall jet could be made visible by using a smoke wire after the efflux velocity was considerably reduced. The three streaklines seen in the photograph (figure 15*b*) originated in the potential core of the jet. The roll-up occurred further from the nozzle and it clearly shows the double structure of the eddies associated with the outer and inner regions of the wall jet. The eddy structure near the surface could be interpreted in terms of the terminology suggested by Kline *et al.* (1967) for the coherent structures observed in the turbulent boundary layer. One may indeed see high-speed sweeps towards the wall being interspersed by ejections of fluid from the wall. The outer eddies, which are characteristic of a plane jet, reside above the ejected fluid of the inner structures, providing constructive induction for the ejected fluid. This double structure of eddies stems from the shape of the wall-jet profile (as provided by Glauert's 1956 solution) which can support the coexistence of two instability eigenmodes. The structures observed in figure 15(*b*) were predicted by Tsuji *et al.* (1977) who solved the Orr–Sommerfeld equations for Glauert's profile. Although the flow in the turbulent wall jet is different, because of

the existence of three-dimensional vorticity fluctuations which are omnipresent in turbulent flows and because of the relative thinness of the inner boundary layer, a qualitative similarity between the observations made in figures 15(*a*) and 15(*b*) does exist. The existence of two rows of vortices in turbulent flow is, however, doubtful. It seems that the large eddies observed in figure 15(*a*) extend from the surface to the outer flow. Thus the turbulent wall jet, cannot be analysed as if it consisted of two independent flows which are merely superposed one on top of the other, and the idea of strip integration may have to be revised.

3.3. *The application of linear stability analysis to the turbulent wall jet*

The propagation and amplification of small-amplitude wavy disturbances, in slightly divergent free shear flows has been discussed by Crighton & Gaster (1976), Gaster, Kit & Wygnanski (1985), Cohen & Wygnanski (1987), and others. The application of this analysis to the wall jet is, in principle, the same, with the exception of the 'no-slip' boundary conditions at the wall and the need to use the viscous form of the Orr–Sommerfeld equation. This problem was also analysed by Gaster (1974) in conjunction with the stability of the divergent boundary layer. The stability of the non-divergent laminar wall jet was considered by Tsuji *et al.* (1977). We shall, therefore, not repeat these derivations and only dwell on the specific aspects (or difficulties) stemming from the application of this model to the turbulent wall jet.

First, one has to define the measured mean velocity distribution with maximum precision possible, because both U and U'' (i.e. the second derivative of the velocity with respect to Y) are needed as inputs into the Orr–Sommerfeld equation. The outer part of the wall jet can be easily described analytically using conventional similarity variables but to fit an analytic function for the inner region is not a simple task because of the very steep gradients involved. These difficulties are further compounded by the fact that the inner part of the velocity profile is dependent on Reynolds number. The analytic description suggested by J. Cohen takes the following form:

$$\bar{U} = \begin{cases} A\tanh(\eta_1) + Q\dfrac{\ln(\eta_2)}{\eta_2} & \text{for} \quad y \leqslant y_{\mathrm{m}}, \\ \left[2\left(\dfrac{y}{y_{\mathrm{m}}}\right)^{p} - \left(\dfrac{y}{y_{\mathrm{m}}}\right)^{2p}\right]\exp\left[-D(y-y_{\mathrm{m}})^2\right] & \text{for} \quad y \geqslant y_{\mathrm{m}}, \end{cases} \tag{3.4}$$

where $$\bar{U} \equiv \frac{U}{U_{\mathrm{m}}}; \quad y \equiv \frac{Y}{Y_{\mathrm{m}/2}}; \quad \eta_1 \equiv K\frac{y}{(y_{\mathrm{m}}-y)^{\frac{1}{2}}}; \quad \eta_2 \equiv 1+(e-1)\frac{y}{y_{\mathrm{m}}}.$$

Note that the no-slip condition at the wall, as well as the disappearance of viscous stress at y_{m}, are implicitly satisfied by the virtue of the above definition of $\bar{U}$ (i.e. $\bar{U}(0) = 0$ and $(\mathrm{d}\bar{U}/\mathrm{d}y)(y_{\mathrm{m}}) = 0$).

The five parameters; A, Q, p, D, K are determined by the following boundary conditions:

(i) $$\frac{\mathrm{d}\bar{U}}{\mathrm{d}y}(y=0) = C > 0,$$

where C is a given slope,

(ii) $$\frac{\mathrm{d}^2\bar{U}}{\mathrm{d}y^2}(y=0) = 0,$$

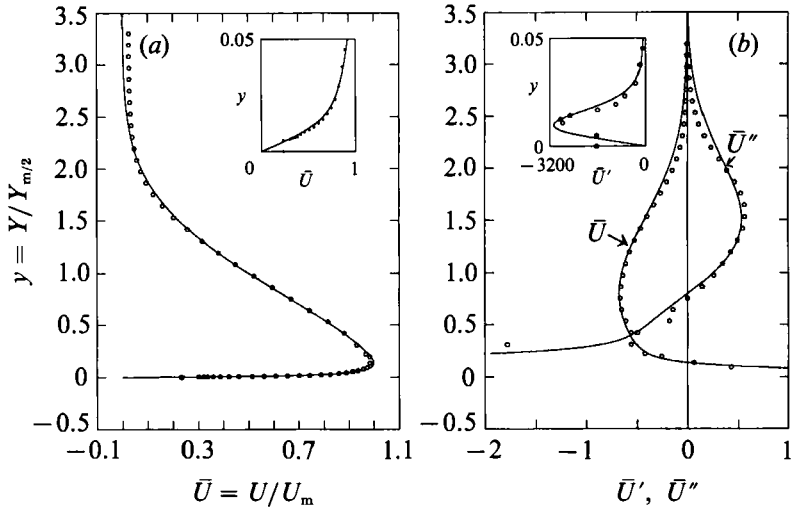

FIGURE 16. An analytic representation of (*a*) the velocity profile and (*b*) its two derivatives as used in the stability calculations.

(iii) $$\bar{U}(y_m^-) = \bar{U}(y_m^+) = 1,$$

(iv) $$\frac{d^2\bar{U}}{dy^2}(y_m^-) = \frac{d^2\bar{U}}{dy^2}(y_m^+),$$

(v) $$\bar{U}(y = 1) = \tfrac{1}{2}.$$

This empirical description of the velocity profile fits the data well (figure 16) and satisfies the need for a continuous second derivative which vanishes at the surface because of the absence of pressure gradient. The variation of $\bar{U}''$ very near the surface is shown in the insert to figure 16. It indicates that $\bar{U}''$ increases by three orders of magnitude (to a level of -3200) within $0 < (Y/Y_{m/2}) < 0.01$. The abrupt increase in $\bar{U}''$ poses a major difficulty in calculating the linear stability characteristics of the turbulent wall jet. The need for a precise definition of $\bar{U}''$ is also stressed by Tsuji *et al.* (1977) who compared the stability of a laminar wall jet with the stability of the flow resulting from laminar free convection along a vertical flat plate. Although both velocity profiles look alike, their stability characteristics are different because Glauert's (1956) solution has an inflexion point at the wall which gives rise to another eigenmode of instability at $Re_m \equiv U_m Y_{m/2}/\nu > 300$. We did not find another unstable mode for the velocity profile described above. This might be attributed to the very steep gradients encountered (figure 16) and our inability to resolve the gradients in $\bar{U}''$ with an adequate accuracy. The possible existence of another instability mode should not, however, be ruled out.

The perturbation stream function initially assumed for the locally parallel mean flow is given by

$$\psi(y,t) = \phi(y)\exp[\mathrm{i}(\alpha x - \beta t)], \tag{3.5}$$

where $$x = \frac{X}{Y_{m/2}}, \quad y = \frac{Y}{Y_{m/2}}, \quad t = \frac{TU_m}{Y_{m/2}}, \quad \psi = \frac{\Psi}{U_m Y_{m/2}}.$$

The eigenfunction $\phi(x,y)$ satisfies the Orr–Sommerfeld equation:

$$(\bar{U}-c)(\phi''-\alpha^2\phi) - \bar{U}''\phi + (\mathrm{i}/\alpha R)[\phi^{\mathrm{iv}} - 2\alpha^2\phi'' + \alpha^4\phi] = 0 \tag{3.6}$$

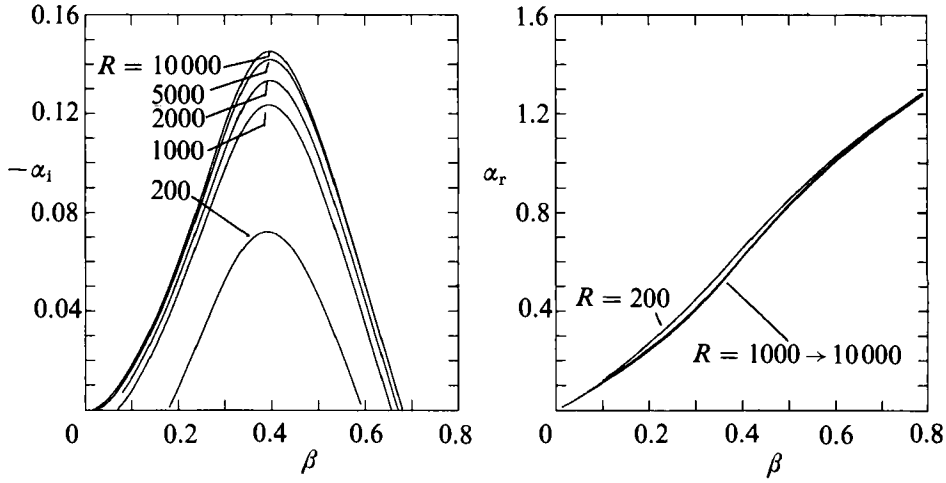

FIGURE 17. The computed α_i and α_r as functions of the dimensionless frequency β keeping $R = U_m Y_{m/2}/\nu$ as a parameter.

subject to the boundary conditions

$$\phi(y=0) = \phi(y=\infty) = 0, \quad \frac{\partial\phi}{\partial y}(y=0) = \frac{\partial\phi}{\partial y}(y=\infty) = 0,$$

because (3.6) is solved locally for each $U(x, y)$. A real frequency parameter $\beta(x) \equiv [2\Pi f Y_{m/2}/U_m]$ and a complex wavenumber $\alpha(x)$ are the eigenvalues of the equation determining the phase velocity $c = \beta/\alpha$ for a given Reynolds number

$$R = Re_m \equiv U_m Y_{m/2}/\nu.$$

A Gram–Schmidt orthonormalization procedure was used to solve the equation because the coefficient $(i/\alpha R)$ multiplying the highest derivative in (3.6) is very small.

One starts the solution process by guessing $\alpha(x)$ and improving on the guess until the boundary conditions are satisfied. Since this 'shooting' procedure is very sensitive to the initial guess of α, the latter was obtained by solving the inviscid equation first although it did not satisfy the boundary conditions at the wall. The eigenvalues determined from the solution of (3.6) which correspond to the complex wavenumber are plotted in figure 17 as functions of the real frequency parameter for a variety of Reynolds numbers. The plotted solutions bracket the range of frequencies in which the perturbation is amplified (i.e. $\alpha_i < 0$). One may observe that the real part of α is almost independent of Reynolds number while the imaginary part of α is weakly dependent on R beyond $R > 1000$. These results provide an explanation for the success of the inviscid equation in predicting α. They also help in identifying the relationship between the large coherent structures in the wall jet and the instability modes. One may expect the predominant frequency of the large coherent eddies to correspond to $\beta \approx 0.6$ since this is the frequency at which these eddies completed their amplification cycle. Furthermore the expected celerity of the large coherent structures is approximately $0.6U_m$.

The effect of the slight divergence of the mean flow may be accounted for by modifying the perturbation stream function to the form

$$\psi(x, y, t) = A_0\phi(x, y) \exp\left[\int_{x_0}^{x}\left[i\alpha(x) - \frac{N(x)}{M(x)}\right]dx - i\beta t\right] \tag{3.7}$$

where now $$x = \frac{X}{b}, \quad y = \frac{Y}{b}, \quad t = \frac{TU_j}{b}, \quad \psi = \frac{\Psi}{U_j b}.$$

A_0 is an arbitrary constant determined to give

$$\int_0^\infty A_0 |\phi_y(\beta, y)| \, dy = 1 \quad \text{at} \quad x = x_0.$$

Substituting (3.7) into the equations of motion yields the Orr–Sommerfeld equation (3.6) to the first level of approximation at a given coordinate x, which is considered as a parameter. In the present equation all velocities and lengths are scaled with U_j and b respectively while $R = Re_j \equiv U_j b/\nu$ (e.g. $\bar{U}$ in the current form is actually $\bar{U}$ of (3.4) times U_m/U_j.

The solvability condition provides the solution for $N(x)$ and $M(x)$ which reflect the non-parallel effects on the overall amplification:

$$N(x) = \int_0^\infty \varphi \Big\{ \alpha_x(\beta - 3\bar{U}\alpha)\phi + [2\alpha\beta - 3\bar{U}\alpha^2 - \bar{U}_{yy}]\phi_x + \bar{U}\phi_{xyy} + \bar{U}_{xy}\phi_y + \bar{V}(\phi_{yyy} - \alpha^2\phi_y) - \frac{2i}{R}[\alpha_x(\phi_{yy} - 3\alpha^2\phi) + 2\alpha(\phi_{xyy} - \alpha^2\phi_x)] \Big\} dy, \quad (3.8)$$

$$M(x) = \int_0^\infty \varphi \Big\{ [2\alpha\beta - 3\bar{U}\alpha^2 - \bar{U}_{yy}]\phi + \bar{U}\phi_{yy} - \frac{4i\alpha}{R}[\phi_{yy} - \alpha^2\phi] \Big\} dy, \quad (3.9)$$

and φ is the adjoint eigenfunction satisfying

$$(\bar{U} - c)[\varphi_{yy} - \alpha^2\varphi] + 2\bar{U}_y\varphi_y + \frac{i}{\alpha R}[\varphi_{yyyy} - 2\alpha^2\varphi_{yy} + \alpha^4\varphi] = 0, \quad (3.10)$$

which is solved together with (3.6).

3.4. *On the possible relationship between large coherent structures and the predominant instability modes*

The identification of the large coherent structures with the predominant instability modes of the mean motion is accomplished in part by resorting to spectral methods. Power spectral densities of the streamwise component of the velocity fluctuations were measured at several streamwise locations in the flow ranging from $X/b = 30$ to 100. The measurements presented in figures 18(*a*) and 18(*b*) represent data taken near the surface ($Y/Y_{m/2} \approx 0.15$ where $U/U_m \approx 1$), while data acquired near the outer edge of the wall jet ($Y/Y_{m/2} = 1.8$ where $U/U_m \approx 0.1$) are plotted in figures 18(*c*) and 18(*d*). In order to accentuate the characteristic frequency associated with the passage of the large eddies, the abscissa on this figure represents frequency plotted on a logarithmic scale while the ordinate represents the power spectrum F multiplied by the frequency in order to equipartition the contribution of each frequency to the total turbulent energy [i.e. $\overline{u'^2} \propto \int F(f)\,df = \int fF(f)\,d(\log f)$]. Only the most significant decade of each spectrum has been plotted. One may observe that the predominant frequency decreases in the direction of streaming in conjunction with the broadening of the jet and a decrease in its maximum velocity. These power spectra become approximately self-similar when they are replotted against β (figure 18*b*, *d*), which represents the dimensionless frequency governing the linear stability of this flow. Furthermore, the peak in the spectrum measured at the outer part of the wall jet (figure 18*d*) corresponds to $\beta \approx 0.5$ which is in the neighbourhood of the

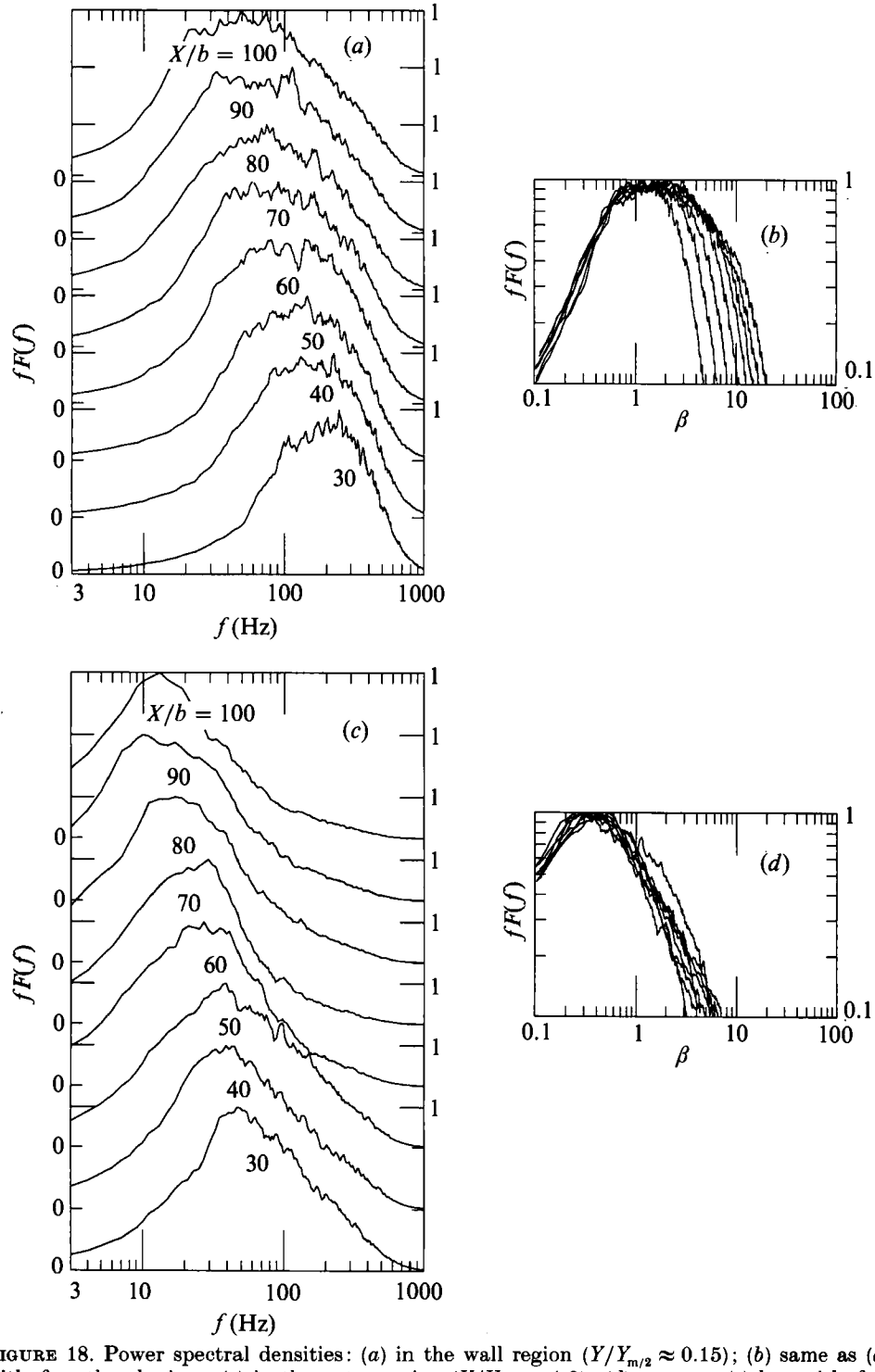

FIGURE 18. Power spectral densities: (*a*) in the wall region ($Y/Y_{m/2} \approx 0.15$); (*b*) same as (*a*) but with β as the abscissa; (*c*) in the outer region ($Y/Y_{m/2} \approx 1.8$); (*d*) same as (*c*) but with β as the abscissa.

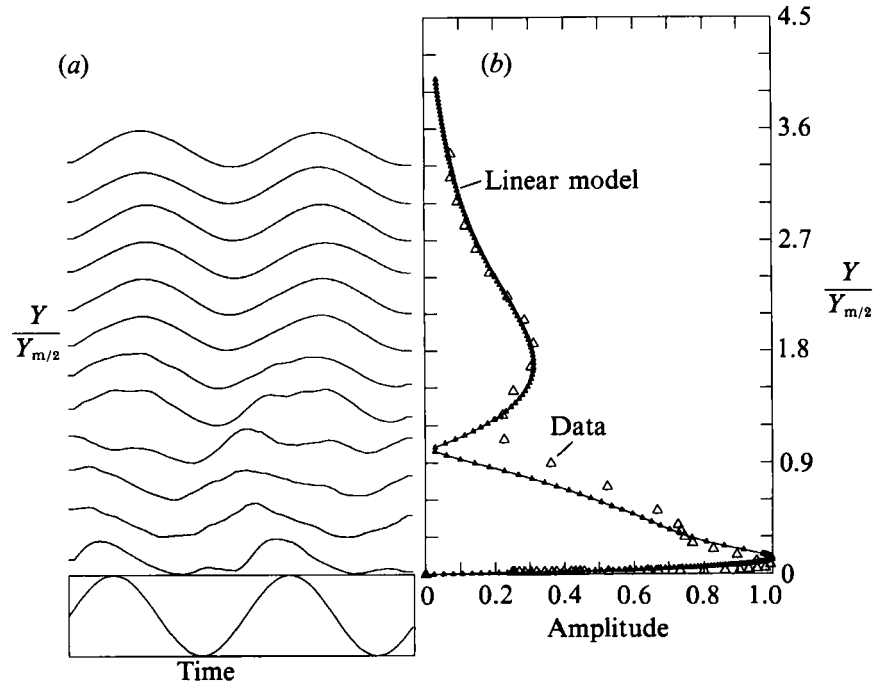

FIGURE 19. (*a*) Phase-locked and ensemble-averaged velocity traces across the jet plotted together with the forcing signal. (*b*) A comparison between the amplitude calculated using the linear stability theory and the ensemble-averaged amplitude measured in the flow at the imposed (fundamental) frequency.

frequency which might have undergone the highest possible linear amplification, suggesting that the large eddies observed in the outer part of the unexcited turbulent wall jet might be represented by the most amplified spatial normal modes.

The power spectrum measured very close to the surface (figure 18*b*) peaked near the first harmonic frequency of the predominant power spectrum in the outer flow and the drop-off at the higher frequencies did not scale with β. This might be due to some nonlinear effects which are more prominent near the surface or perhaps due to the existence of another mode of instability (Tsuji *et al.* 1977). Nevertheless, there is sufficient reason to believe that the primary large coherent structures existing in this wall-bounded flow are related to the most unstable linear modes in a fashion similar to that in free shear flows.

3.5. *The evolution of harmonic perturbations in the wall jet*

Harmonic excitation of the wall jet enabled us to digitize the measured velocities at any streamwise location, together with the forcing signal which was used to deflect the flap or to change the displacement volume in the settling chamber. This signal (plotted at the bottom left corner of figure 19*a*) provided the necessary phase reference with respect to which other measurements taken anywhere in the flow could be referred and ensemble averaged. Since there is a possibility of a subharmonic resonance, the long-time series were subdivided into segments which contain two waves of the forcing frequency. Such phase-locked and ensemble-averaged traces of the streamwise component of velocity taken at $X/b = 60$ and $Y/Y_{m/2}$ ranging from 0.016 to 3.6 are plotted above the forcing signal on figure 19(*a*). The periodicity of this signal is self-evident but its harmonic distortion varies with Y. The least

distorted signals appear at the outer edge of the flow where the velocity is not contaminated by turbulence. One may observe a slow phase advance in the maximum velocity recorded with increasing distance from the wall provided $Y/Y_{m/2} < 1$. At this Y-location, which approximately coincides with the inflexion point of the mean velocity profile, a sudden phase shift occurs which is followed by a gradual phase delay with increasing Y. One may Fourier decompose these signals and plot the transverse distributions of amplitude and phase of the signals at the frequency of forcing. The transverse distribution thus obtained, may be compared with the amplitude and phase distributions calculated from the linear stability model. An example of such a local comparison is shown in figure 19(*b*) where an amplitude calculated by solving the Orr–Sommerfeld equation is plotted. Both measured and calculated amplitude distributions are normalized by their local maximum which occurs fairly close to the wall.

When a similar comparison was done in highly unstable, unbounded turbulent shear flows like the mixing layer, the interaction between the coherent motion and the incoherent turbulence was not accounted for. Since these flows were dominated by an inviscid instability the inviscid Orr–Sommerfeld equation was solved, and the role of the Reynolds number did not have to be considered. The lateral distribution of the phase-locked fluctuations at the imposed frequency agreed very well with the results extracted from the eigenfunctions satisfying the inviscid equations (e.g. see the comparisons made by Weisbrot & Wygnanski 1988 for the case of a turbulent mixing layer). The primary instability in the wall jet is affected by viscosity in spite of the fact that the outer region of the wall jet is inviscidly unstable. The no-slip condition at the surface not only modifies the shape of the computed eigenfunctions but also provides viscous stresses and enhances the dissipation which may cause an earlier decay of the harmonic motion. The incoherent turbulent fluctuations may increase this dissipation and the nonlinear interactions between the coherent and incoherent fluctuations may provide a cascade mechanism through which the effects of viscosity are enhanced. All these interactions, which are not accounted for in the model, might be lumped together into an equivalent viscous term by introducing an eddy viscosity (see also Liu 1971; Tam & Chen 1979; Marasli, Champagne & Wygnanski 1989). Since the Reynolds number appears as a parameter in the Orr–Sommerfeld equation a choice of fictitious Re introduces an indeterminacy not present in the inviscid calculations. For example, the experimental results plotted in figure 19, which were taken at $Re_m = 10^4$, agree reasonably well with the theoretical model provided that the eddy viscosity is 10 times larger than the viscosity of the fluid (i.e. the selected Re was 10^3). It should be stressed that the choice of an eddy viscosity is arbitrary and may not be related to any physical mechanism existing in the flow. In other examples, the ratio between actual and the selected Reynolds numbers providing the best agreement with the model was different.

In order to examine the streamwise evolution of a disturbance with some degree of consistency we selected an initial value for the eddy viscosity and assumed that

$$\nu_\tau \propto U_m Y_{m/2}. \tag{3.11}$$

This assumption is at least equivalent to the initial normalization of the amplitudes by the amplitude measured at the initial X-location. A comparison between the measured and the calculated amplitude and phase distribution based on the slightly divergent model, proposed in equations (3.6)–(3.10) is shown in figure 20(*a*, *b*). The initial ratio of ν/ν_τ selected was approximately 5.2% (at $X/b = 30$ where $U_j b/\nu_\tau = 530$) and each amplitude in the figure was normalized by its local maximum

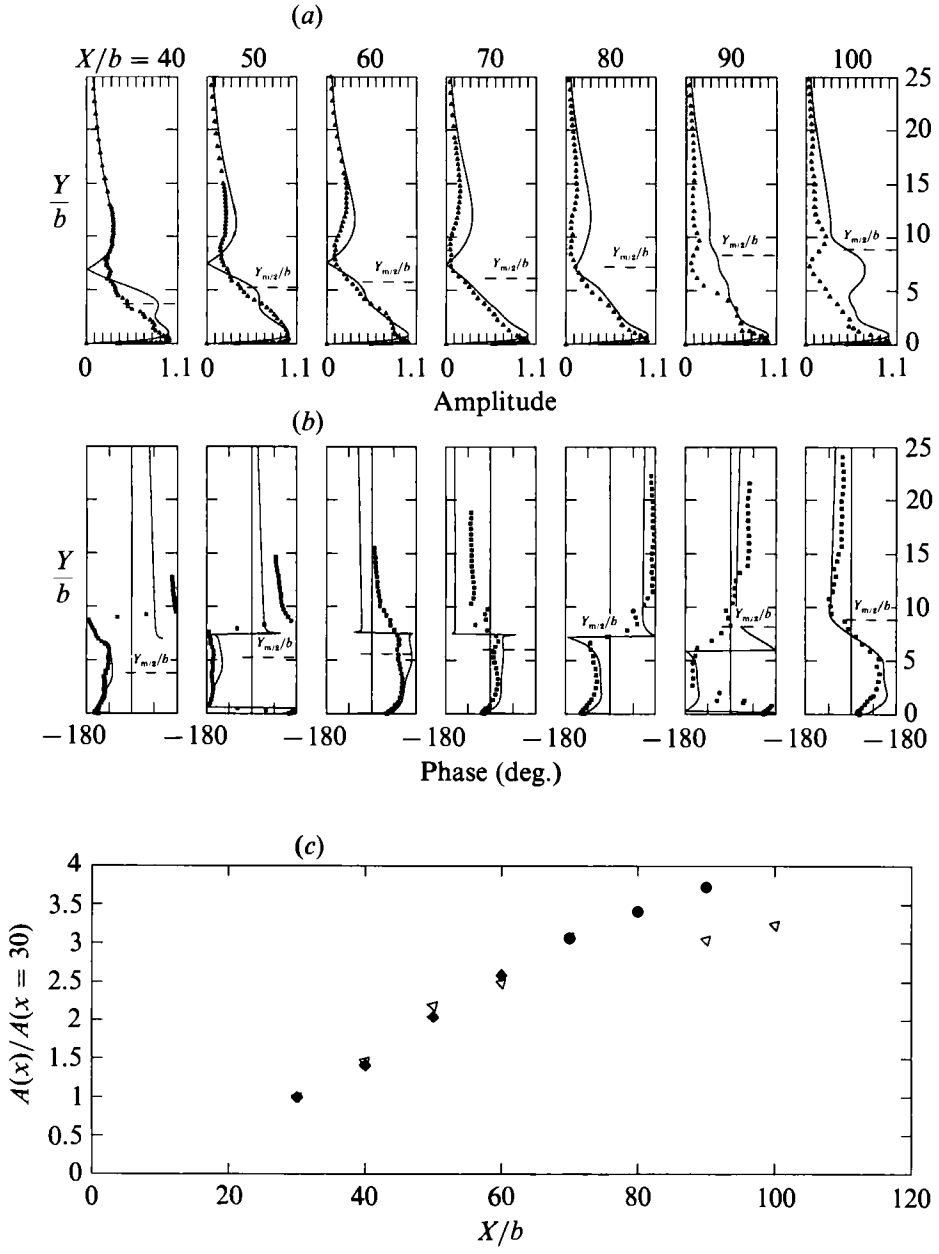

FIGURE 20. (*a*) Amplitude and (*b*) phase distributions in the forced wall jet – a comparison of a linear model with experiment. (*c*) The amplification of the forced wave with X: ◆, non-parallel theory; ◁, experiment.

amplitude measured at the given X-location. Note that the definition (3.11) yields a constant $R = U_m Y_{m/2}/\nu_T$ at all X-locations. The lateral distribution of amplitudes across the flow is reasonably well represented by the model but the agreement between 'theory' and experiment is inferior to the agreement achieved in free shear flows (e.g. the mixing layer – Weisbrot & Wygnanski 1988; the plane wake – Marasli *et al.* 1989). This may stem from the fact that in the free shear flows mentioned, the

shape of the normalized mean velocity distribution is insensitive to the forcing and it does not even change when the flow undergoes transition from a laminar to a turbulent state. The velocity profile in the inner portion of the wall jet is distorted by strong perturbations, as best witnessed by the difference between laminar and turbulent profiles (e.g. Tsuji *et al.* 1977). Mean flow distortion by the primary instability makes the velocity profile susceptible to a secondary instability which might have a very different eigenfunction associated with it. This susceptibility was not investigated here.

The overall amplification ratio of the integrated amplitudes across the flow,

$$A(x,f)_{\text{experimental}} = \frac{1}{A(x_0,f)} \int_0^\infty \langle u \rangle'(x,y,f)\,\mathrm{d}y, \tag{3.12}$$

was compared to the amplification obtained from the slightly divergent model,

$$A(x,f)_{\text{model}} = \int_0^\infty A_0 |\phi'(x,y)| \exp\left[-\int_{x_0}^x \left[\alpha_i(\xi) + \left(\frac{N(\xi)}{M(\xi)} \right)_r \right] \mathrm{d}\xi \right] \mathrm{d}y. \tag{3.13}$$

The comparison is plotted on figure 20(*c*). One can deduce that the amplification of harmonic disturbances in the direction of streaming is fairly well predicted by the linear model. This was not the case when the inviscid model was applied to free shear flows (e.g. Gaster *et al.* 1985). The current improvement in the prediction is attributed to the inclusion of eddy viscosity which may account for turbulent dissipation by reducing the effective Re and, through it, the amplification rate in the streamwise direction.

3.6. *The modification of large coherent structures by two-dimensional excitation of the flow*

In this section we shall explore the changes that took place in the large-scale structures in response to the external excitation. We shall particularly look for effects taking place near the solid surface in order to ascertain the reasons for the reduction in τ_w. The improvement in the two-dimensionality of the large-scale structures is one such effect which had been observed in both the mixing layer and in the wake (Wygnanski *et al.* 1979; Wygnanski, Champagne & Marasli 1986).

The coherence spectra calculated from 'n' buffers of the velocity fluctuations, sensed by two probes separated in the spanwise direction is given by

$$\mathrm{Coh}\,(\Delta Z,f) \equiv \frac{\left[\left| \sum_{i=1}^{n} F_i(0,f)\,F_i(\Delta Z,f) \right| \right]^2}{\sum_{i=1}^{n} |F_i(0,f)|^2 \sum_{i=1}^{n} |F_i(\Delta Z,f)|^2} \tag{3.14}$$

and provides a convenient measure of the degree of two-dimensionality attributable to each scale (or frequency) of the motion. Two-point correlations of the broad-frequency signal also yield a measure of two-dimensionality which is biased somewhat towards the most energetic eddies. The data plotted in figure 21 represent coherence at spanwise separation distances ranging from 50 to 125 mm (corresponding to $\Delta Z/Y_{m/2}$ varying from 2 to 5). The measurements were done across the entire wall jet, at X/b 30, in the presence and in the absence of external excitation. The frequency chosen to be shown was 34 Hz corresponding to $St = fv^3/J^2 = 88 \times 10^{-15}$. The results plotted in figure 21 correspond to four Y-locations: starting at the outer edge of the wall jet ($Y/Y_{m/2} \approx 2$), proceeding to the vicinity of the inflexion

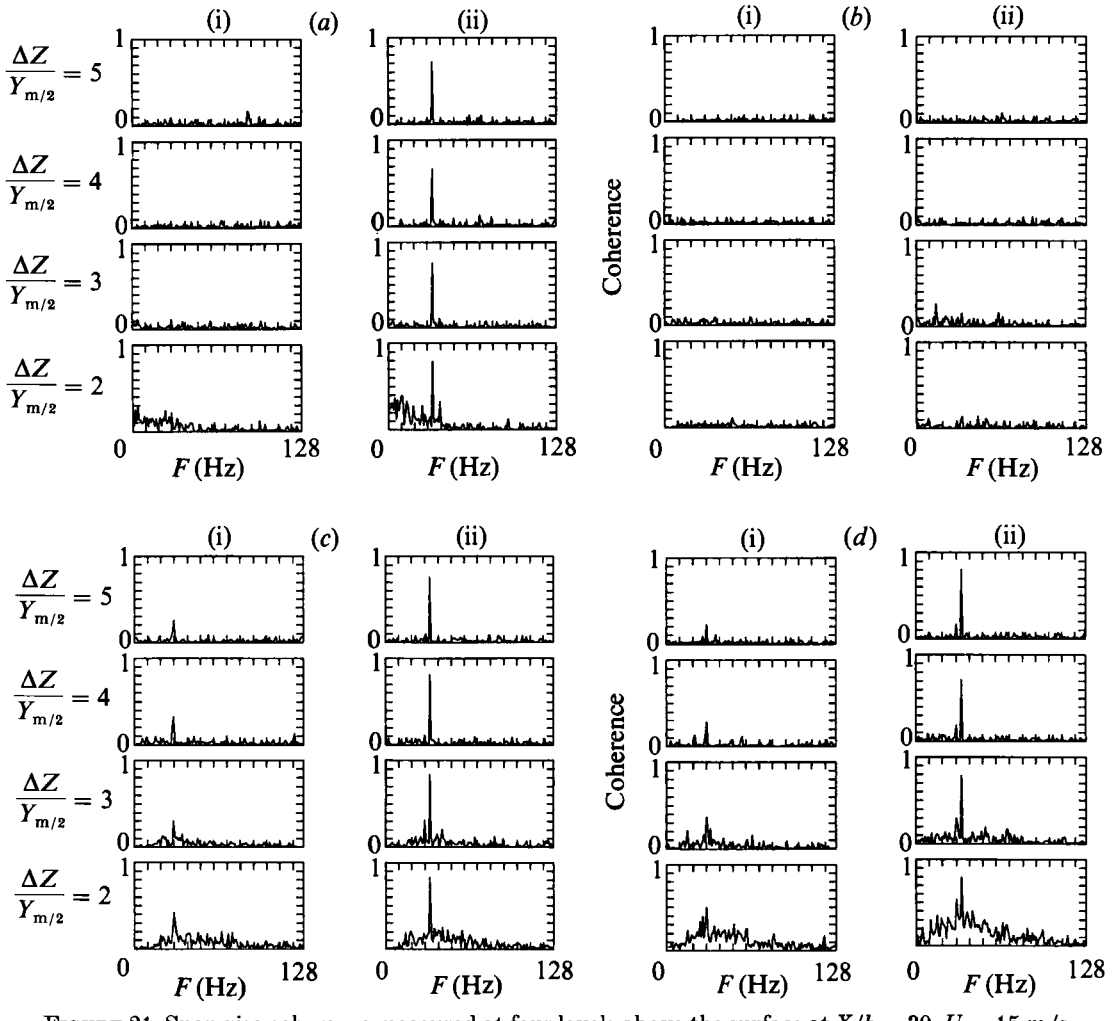

FIGURE 21. Spanwise coherence measured at four levels above the surface at $X/b = 30$, $U_j = 15$ m/s, $Re_j = 5000$. (*a*) $Y/Y_{m/2} \approx 2$, $U/U_m \approx 0.1$; (*b*) $Y/Y_{m/2} \approx 1$, $U/U_m \approx 0.5$; (*c*) $Y/Y_{m/2} \approx 0.15$, $U/U_m \approx 1$; (*d*) $Y/Y_{m/2} \approx 0.01$, $U/U_m \approx 0.5$. (i) Unforced; (ii) forced at 34 Hz, $St \times 10^{15} = 88$.

point of the mean velocity profile ($Y/Y_{m/2} \approx 1$), going down to the location at which $U \approx U_m$ and ending in the vicinity of the wall. The spanwise coherence in the outer part of the unforced jet is negligible provided $\Delta Z/Y_{m/2} > 2$ (figure 21*a*). For $\Delta Z/Y_{m/2} \leqslant 2$ the coherence in the unforced flow exceeds the value of 0.15 over a broad range of low frequencies and Y-locations, suggesting that the large-scale structures occurring naturally in the flow are somewhat coherent over this span. There is also a distinct peak in the coherence level at around 30 Hz ($St \times 10^{15} = 78$ see figure 21*c*, *d*) which is noticeable even when $\Delta Z/Y_{m/2} = 5$ within the inner part of the unforced wall jet. If this St is associated with the natural coherence of the large eddies, then the forcing frequency used in the experiment is very close to being the frequency which undergoes, naturally, the highest level of amplification at this particular X-location.

External excitation increased the spanwise coherence to 0.75 at the outer edge of the wall jet (figure 21*a*) but failed to have any effect near $Y/Y_{m/2} = 1$ (figure 21*b*). This effect may be explained with the aid of figure 19 which is representative of the

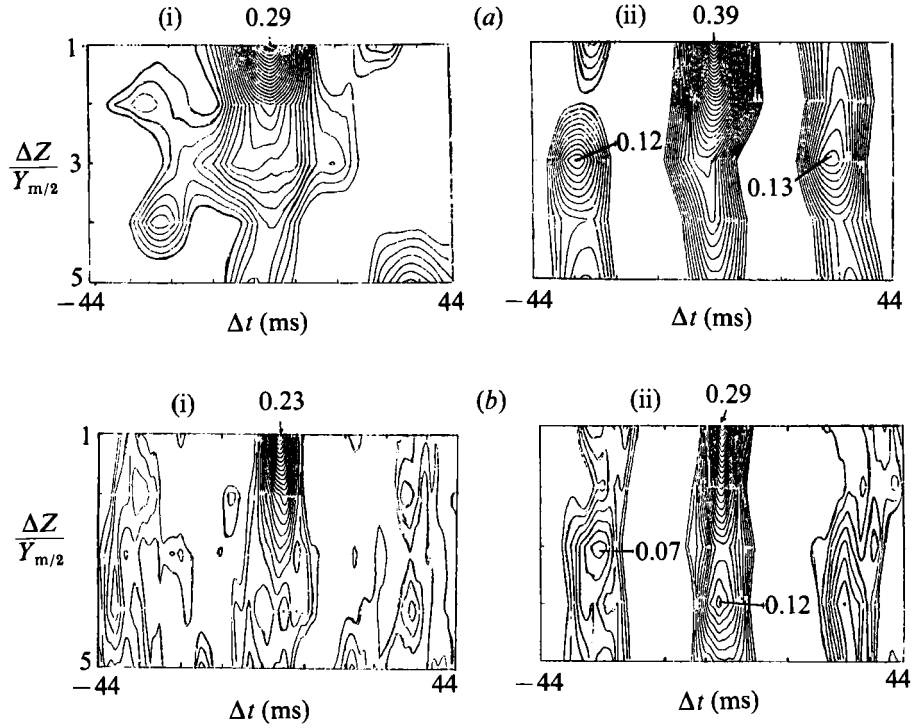

FIGURE 22. Two-point correlation measurements plotted in the (t, Z)-plane, (a) in the outer region of the flow, $Y/Y_{m/2} = 1.8$, $U/U_m = 0.1$; (b) near the surface, $Y/Y_{m/2} = 0.01$, $U/U_m = 0.5$, (i) Unforced, (ii) forced at 34 Hz.

coherent amplitude distribution of the streamwise velocity fluctuations in the forced wall jet. The maximum amplitude of the coherent motion in the outer part of the jet occurs around $Y/Y_{m/2} = 1.8$ while the minimum occurs at $Y/Y_{m/2} = 1$, and therefore one should not expect any improvement in the coherence in the vicinity of this Y-location. The improvement in the coherence observed in the inner region of the wall jet (at $Y/Y_{m/2} = 0.15$ and 0.01) can also be associated with the relatively large amplitude of the imposed oscillations. It is interesting to note that the spanwise coherence in the forced wall jet did not diminish on increasing ΔZ and it was actually higher near the surface than in the outer edge of the jet.

Contour plots of the correlation coefficient

$$\mathrm{Cor}\,(\Delta Z, \Delta t) \equiv \frac{\int_{-\infty}^{\infty} u'(0,t)\,u'(\Delta Z, t+\Delta t)\,\mathrm{d}t}{\left[\int_{-\infty}^{\infty} u'(0,t)^2\,\mathrm{d}t\right]^{\frac{1}{2}}\left[\int_{-\infty}^{\infty} u'(\Delta Z,t)^2\,\mathrm{d}t\right]^{\frac{1}{2}}} \tag{3.15}$$

taken at $Y/Y_{m/2} = 1.8$ and 0.01 are shown in figure 22(a) and 22(b) for the forced ($St = f\nu^3/J^2 = 88 \times 10^{-15}$) and unforced flows investigated at $Re_j = 5000$. The minimum separation distance for these data was 25 mm. The contour plots representing the natural flow exhibit some periodic behaviour particularly near the surface (figure 22b). One may also detect a preferred spanwise wavelength of $\Delta Z/Y_{m/2} = 2$ in the outer region of the jet.

Forcing the wall jet not only increased the spanwise extent of the highly correlated region but made it much more periodic in time. The primary eddies appear to be two-

dimensional and regular, but a susceptibility to spanwise modes is also apparent. For instance at $Y/Y_{m/2} = 1.8$, the local maximum correlation measured at $\Delta t = \pm 30$ ms is displaced by $\Delta Z/Y_{m/2} = 3$ relative to the maximum correlation measured at $\Delta t = 0$ and $\Delta Z = 0$. A similar though less clear observation may be made near the surface. These results point to the possibility that two spanwise modes interact in a resonant fashion with a fundamental two-dimensional mode to produce a staggered (subharmonic) three-dimensional pattern. This process, which contributes to the destabilization of the laminar boundary layer, might also be responsible for the limited spanwise extent of the primary eddies in the wall jet and for the limited success of the linear stability model in predicting the two-dimensional coherent motion.

One may proceed to investigate the secondary instability of the forced wall jet on the basis of these preliminary observations, but this aspect is not contemplated in the immediate future unless numerical simulation (H. Fasel 1990, personal communication) indicates that this is an important mechanism governing the distortion of the large eddies. Nevertheless, the unexpected reduction in the mean skin friction prompted us to examine the phase-locked distribution of this quantity over two periods of the forcing frequency. The data plotted in figure 23 are based on the phase-locked analysis of $[\partial\langle U\rangle/\partial Y]_w$ measured at various streamwise locations. The oscillations in the skin friction correspond to the oscillations imposed on the flow, and their average is represented by a solid horizontal line on the figure. The dashed line represents the wall stress measured in the absence of forcing, and thus the difference between these two lines indicates the local reduction in τ_w. It is interesting to note that the maximum skin friction observed during any phase of the forced oscillation at any streamwise location corresponds approximately to the mean skin friction of the unforced flow (figure 23).

4. Conclusions

Two-dimensional excitation of the plane turbulent wall jet in the absence of an external stream has no appreciable effect on the rate of spread of the jet nor on the decay of its maximum velocity. In fact the mean velocity distribution plotted in the conventional similarity coordinates is not altered by the external excitation in any obvious manner. Careful examination of the flow near the surface (i.e. for $0 < Y^+ < 100$) reveals some profound differences which manifest themselves in reducing the skin friction. Local reductions of 30% in the wall stress, as a consequence of such an excitation, were not uncommon. The skin-friction drag, which is the only contributor to the loss of momentum in this flow, was also reduced by a comparable amount. The production of turbulent energy near the surface was reduced resulting in a lowering of the intensities of the streamwise component of the velocity fluctuations. These effects, which were observed in the fully developed region of the wall jet (i.e. at $X/b > 30$), are insensitive to the method of forcing but they are sensitive to the frequency and the amplitude of the excitation. The outer part of the wall jet was not affected by the excitation, nor was the defect law in the inner region of the flow affected provided the distance from the surface exceeded $Y^+ \approx 30$.

External excitation enhanced the two-dimensionality and the periodicity of the coherent motion. This enhancement is clearly visible near the surface and near the free interface of the turbulent flow. Spectral analysis and flow visualization suggest that the large coherent structures in this flow might be identified with the most-

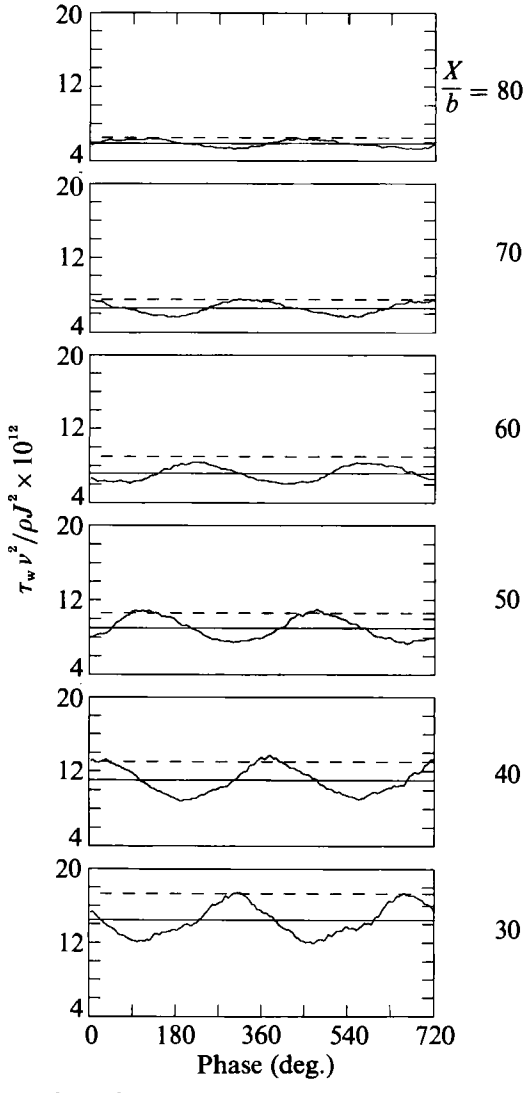

FIGURE 23. The phase dependence of the skin friction at various streamwise locations: ---, unforced; ——, average skin friction with forcing. $St \times 10^{15} = 17$, $Re_j = 7500$.

amplified primary instability modes of the mean velocity profile. Detailed stability analysis confirms this proposition though not at the same level of accuracy as it did in many free shear flows.

The effects of forcing on the other components of the velocity fluctuations will be investigated in future experiments. In particular, the spanwise component of the velocity fluctuations near the surface will be measured in order to explore further the correlation between the improvement in the two-dimensionality of the large-scale motion and the reduction in τ_w. Since most wall-jet applications occur in the presence of an external flow, the next phase of this investigation will incorporate a moving stream in a wind tunnel.

The work was supported in part by a grant from AFOSR (contract number AFOSR-88-0176) and monitored by Dr J. McMichael.

REFERENCES

COHEN, J. & WYGNANSKI, I. 1987 The evolution of instabilities in the axisymmetric jet. Part 1. The linear growth of disturbances near the nozzle. *J. Fluid Mech.* **176**, 191.

CRAIK, A. D. D. 1985 *Wave Interactions and Fluid Flows.* Cambridge University Press.

CRIGHTON, D. G. & GASTER, M. 1976 Stability of slowly diverging jet flow. *J. Flow Mech.* **77**, 397.

FALCO, R. E. 1977 Coherent motion in the outer region of turbulent boundary layers. *Phys. Fluids Suppl.* **20**, 124.

GASTER, M. 1974 On the effects of boundary layer growth on flow stability. *J. Fluid Mech.* **66**, 465.

GASTER, M., KIT, E. & WYGNANSKI, I. 1985 Large scale structures in a forced turbulent mixing layer. *J. Fluid Mech.* **150**, 23.

GLAUERT, M. B. 1956 The wall-jet. *J. Fluid Mech.* **1**, 625.

HO, C. M. & HUERRE, P. 1984 Perturbed free shear layers. *Ann. Rev. Fluid Mech.* **16**, 365.

HUSSAIN, A. K. M. F. & REYNOLDS, W. C. 1970 The mechanics of an organized wave in turbulent shear flow. *J. Fluid Mech.* **41**, 241.

HUSSAIN, A. K. M. F. & REYNOLDS, W. C. 1972 The mechanics of an organized wave in turbulent shear flow. Part 2. Experimental results. *J. Fluid Mech.* **54**, 241.

KATZ, Y., NISHRI, B. & WYGNANSKI, I. 1989 The delay of turbulent boundary-layer separation by oscillatory active control. *AIAA Paper* 89-0975.

KLINE, S. J., REYNOLDS, W. C., SCHRAUB, F. A. & RUNSTADLER, P. W. 1967 The structure of turbulent boundary layers. *J. Fluid Mech.* **50**, 133.

KRUKA, V. & ESKINAZI, S. 1964 The wall-jet in a moving stream. *J. Fluid Mech.* **20**, 555.

LANDAHL, M. T. 1990 On sublayer streaks. *J. Fluid Mech.* **212**, 593.

LAUNDER, B. E. & RODI, W. 1981 The turbulent wall jets. *Prog. Aerospace Sci.* **19**, 81.

LAUNDER, B. E. & RODI, W. 1983 The turbulent wall jet – measurements and modeling. *Ann. Rev. Fluid Mech.* **15**, 429.

LIU, J. T. C. 1971 Nonlinear development of instability wave in a turbulent wake. *Phys. Fluids* **14**, 2251.

MARASLI, B., CHAMPAGNE, F. H. & WYGNANSKI, I. J. 1989 Model decomposition of velocity signals in a plane, turbulent wake. *J. Fluid Mech.* **198**, 255.

NARASIMHA, R., NARAYAN, K. Y. & PARTHASARATHY, S. P. 1973 Parametric analysis of turbulent wall jets in still air. *Aeronaut. J.* **77**, 335.

TAM, C. K. W. & CHEN, K. C. 1979 A statistical model of turbulence in two-dimensional mixing layers. *J. Fluid Mech.* **92**, 303.

TSUJI, Y., MORIKAWA, Y., NAGATANI, T. & SAKOU, M. 1977 The stability of a two-dimensional wall-jet. *Aeronaut. Q.* **XXVIII** (November), 235.

WEISBROT, I. & WYGNANSKI, I. 1988 On coherent structures in a highly excited mixing layer. *J. Fluid Mech.* **195**, 137.

WILLMARTH, W. W. 1975*a* Pressure fluctuations beneath turbulent boundary layers. *Ann. Rev. Fluid Mech.* **7**, 13.

WILLMARTH, W. W. 1975*b* Structure of turbulence in boundary layers. *Advances in Applied Mechanics*, vol. 15 (ed. C.-S. Yih), p. 159. Academic.

WILLS, J. A. B. 1962 The correction of hot-wire readings for proximity to a solid boundary. *J. Fluid Mech.* **12**, 3.

WYGNANSKI, I., CHAMPAGNE, F. & MARASLI, B. 1986 On the large scale structures in two-dimensional, small-deficit, turbulent wakes. *J. Fluid Mech.* **168**, 31.

WYGNANSKI, I., FIEDLER, H., OSTER, D. & DZIOMBA, B. 1979 On the perseverance of a quasi-two-dimensional eddy structure in a turbulent mixing layer. *J. Fluid Mech.* **93**, 325.

WYGNANSKI, I., KATZ, Y. & HOREV, E. 1992 On the applicability of various scaling laws to the turbulent wall jet. *J. Fluid Mech.* **234**, 669 (referred to herein as WKH).

WYGNANSKI, I. & PETERSEN, R. A. 1987 Coherent motion in excited free shear layers. *AIAA J.* **25**, 201.